Gas Shale Anisotropy and Mechanical Property: Laboratory Measurements and Mathematical Modeling

----

A Dissertation Presented to

the Faculty of the Department of Earth and Atmospheric Sciences

University of Houston

In Partial Fulfillment

of the Requirements for the Degree

Doctor of Philosophy

By

Kefei Lu

May 2016

Gas Shale Anisotropy and Mechanical Property: Laboratory Measurements and Mathematical Modeling

Kefei Lu

APPROVED:

Dr. Evgeny M. Chesnokov, Chairman
Department of Geosciences

Dr. John Castagna
Department of Geosciences

Dr. Gennady Goloshubin
Department of Geosciences

Dr. Yasser M. Metwally
Lumina Geophysical, LLC

Dean, College of Natural Science and Mathematics

ACKNOWLEDGEMENTS

I would like to thank my advisor Dr. Evgeny M. Chesnokov and my committee members Dr. John Castagna, Dr. Gennady Goloshubin, and Dr. Yasser M. Metwally for their guidance, valuable remarks, and corrections.

Dr. Evgeny M. Chesnokov, my dissertation supervisor, has provided guidance and contributed many useful suggestions to this dissertation. I appreciate his patient instruction on this dissertation. I want to thank Dr. Yasser M. Metwally for his advice and guidance on my work in the lab. I also want to thank Dr. John Castagna and Dr. Gennady Goloshubin for their useful comments, suggestions, and encouragement in my study. Special thanks extend to Dr. Nikolay Dyaur for his help and technique support on the ultrasonic velocity measurement, Dr. Tao Jiang and Sharif Morshed for coding the Fortran program of GSA and Di Chen for her work on FIB-SEM microphotographs.

Lastly, thanks to Devon Energy Co. for providing the Barnett shale samples and Marathon Oil Company for offering the Barnett shale dataset.

Gas Shale Anisotropy and Mechanical Property: Laboratory Measurements and Mathematical Modeling

\---

An Abstract of a Dissertation

Presented to

the Faculty of the Department of Earth and Atmospheric Sciences

University of Houston

\---

In Partial Fulfillment

of the Requirements for the Degree

Doctor of Philosophy

\---

By

Kefei Lu

May 2016

ABSTRACT

This dissertation focus on the study of elasticity, permeability, mechanical properties, and the mathematical modeling of Barnett shale. This study is based on the laboratory core measurements, literature data, and data set provided by industry.

We noticed that the difference between assumed 45^o to bedding planes and real cutting angle could reach to 5^o, which leads to more than 15% of C_{13} estimation error. To reduce the angle error, we use both Vp and Vsv measured from core samples to determine the cutting angle and then calculate C_{13} with the real angle, other than traditional way of using Vp at 45^o to calculate C_{13}. This method can be applied to permeability tensor measurements.

Velocity and permeability anisotropy have been measured on 12 core samples. High velocity anisotropy has been observed. P-wave anisotropy parameter ε ranges from 5% to 73% and S-wave parameter γ ranges from 7% to 47% at unconfined conditions. Anisotropy increases with clay and TOC contents increase. Both velocity and permeability reach to the highest values when parallel to bedding planes. The permeability and velocity anisotropy behaviors are the same along the symmetry axis. Permeability is much more sensitive than velocity to the existing anisotropy. Effects are more than 100%.

Literature data and core measurement data from Marathon Oil Company have been analyzed. Shales have Vp/Vs ratios range from 1.5 to 1.8. Besides Vp/Vs ratios, we found that velocities vertical to beddings are closely correlated with those horizontal

to beddings with correlation coefficient 0.61 for both P- and S-wave. This relation may vary from reservoir to reservoir.

The Young's modulus and Poisson's ratios have been calculated in anisotropic formulae and compared with isotropic case for common minerals in shale. For the anisotropic case, negative Poisson's ratios exist at certain direction as reported. Form Marathon data on Barnett core, the static/dynamic Young's modulus ratios range from 0.52 to 0.74. Empirical relations between static and dynamic Young's modulus have been proposed (correlation coefficient for horizontal modulus was 0.81 and for vertical modulus was 0.93, standard errors were 0.16 and 0.05, respectively).

With mineralogy composition and other rock properties, shale medium was estimated using a general singular approximation (GSA). The modeling results fit well with ultrasonic and sonic velocity measurements. The anisotropic Young's modulus and Poisson's ratio calculated from modeled effective elastic constants also show good fit with measured moduli. This means the GSA method can be used to interpret the anisotropic properties of shale reservoirs.

We developed a new method of determining the measuring angle and elastic constant C_{13}. Our measurements showed that permeability anisotropy and velocity anisotropy have good correlation behaviors along the symmetry directions. In respect of Thomson anisotropy parameters, the anisotropic Young's modulus and Poisson's ratios behave differently. In general, results obtained in this study will help to better understand the reservoir structure and stimulate the possibility to predict the unmeasured parameters (permeability) based on measured one (velocity).

CONTENTS

LIST of TABLES

LIST of FIGURES

Chapter 1 Introduction

1.1 Shale

Shale is one of the most common fine-grained sedimentary rocks. Formed from the compaction of silt and clay sized sediments, shale has distinguished finely layered bedding planes (sheet-like parting). Due to its relatively low porosity and permeability, shale works as flow barrier and seal rock to trap oil and gas. Since 1950s, with the development of hydraulic fracturing and horizontal drilling technique, organic shales have become important sources of hydrocarbon.

The Barnett Shale formation is located at the Fort Worth Basin in North Central Texas. It’s a Mississippian-aged shale located at depths of 6,500-8,500 feet below surface. Figure 1-1 shows the stratigraphy of the Fort Worth Basin. The Barnett lies between two limestone units, the underlying Ordovician-age Viola limestone formation and the overlying Pennsylvanian-age Marble Falls limestone formation. In the northeast portion of the Barnett “play area”, the Barnett is split into the upper and lower Barnett by the Forestburg limestone (Montgomery et al., 2005).

In this study, we measured twelve Barnett core samples, provided by Devon Energy Co., for their ultrasonic velocity, permeability tensor, mineral composition, and microstructure. We also analyzed the core and well-log dataset provided by Marathon Oil Company and the literature data for shale core measurement from Vernik and Liu, (1997).

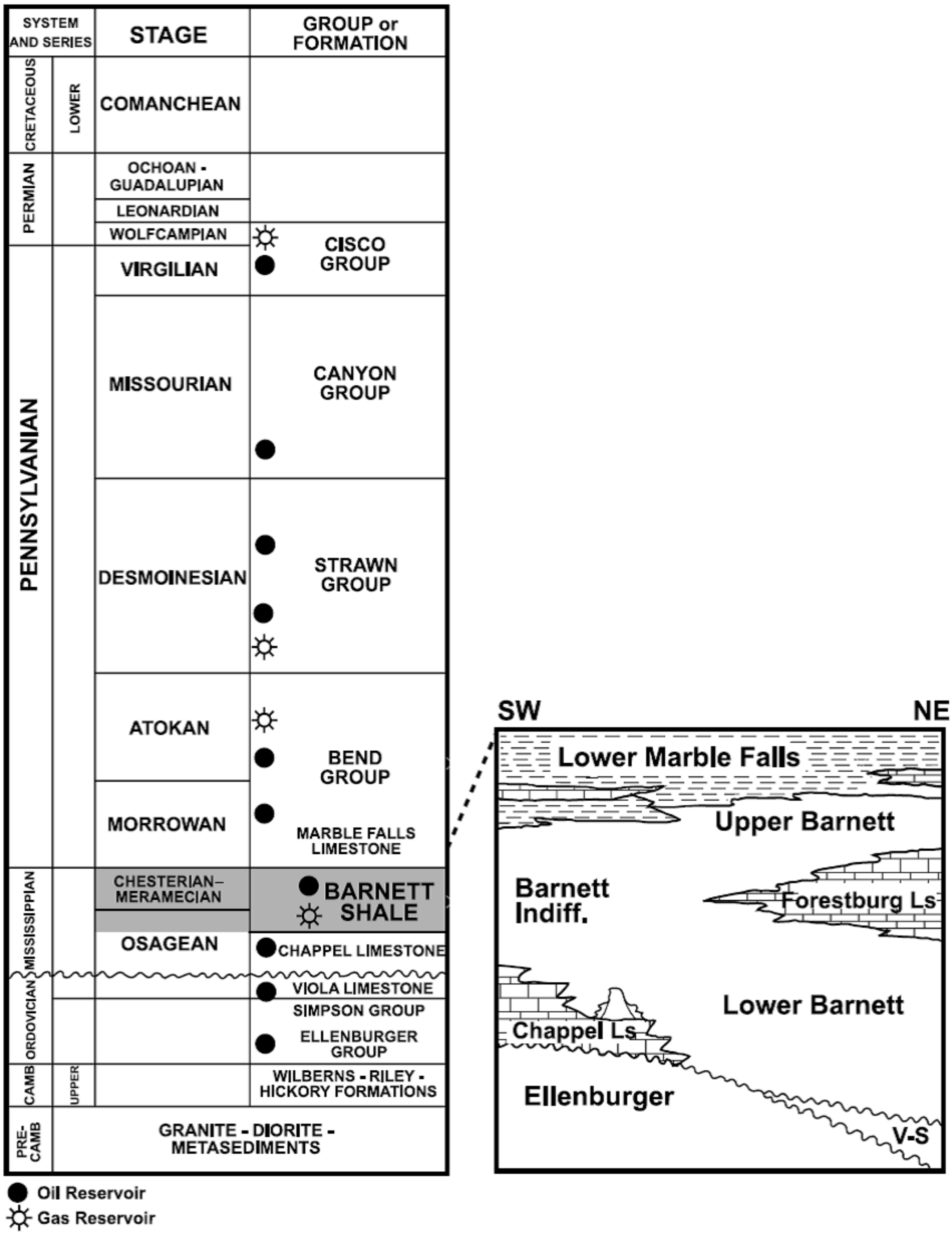

Figure 1-1: Generalized stratigraphy section of the Bend arch – Fort Worth Basin showing the distribution of source, reservoir, and seal rocks of the Barnett- Paleozoic total petroleum system (TPS). (*Figure from the American Association of Petroleum Geologists*)

1.2 Objective of the dissertation

Even though there is a boom of natural gas production from various shale gas reservoirs in North America since 2000, challenges still exist in the exploration of these unconventional reservoirs. Unlike the traditional sandstone reservoir, shale with bedding planes show high anisotropy (Wang, 2002). The anisotropic properties and their application are important for both reservoir analysis and exploration.

Shales are considered as an unconventional type of reservoir (permeability less than 0.1 mDarcy). Therefore, the fluid flow and elastic properties are critical to identify the reservoir's production and recovery potential. Hydraulic fracturing makes shale reservoir feasible for gas production. The prediction of "sweet-spots" and "brittleness" of shale formation in the field requires a deep understanding of the rocks mechanical behaviors.

The main purpose of this dissertation is to study the fundamental problems of shale anisotropy and mechanical properties as porous media. We try to address the following questions in order to enhance our knowledge of shale reservoirs:

1. Can we estimate the anisotropic properties like permeability, Young's modulus, and Poisson's ratio from the elastic wave?
2. What are fundamental controls on the shale anisotropy and mechanical properties?
3. How to simulate the porous media like shale rocks?

1.3 Overview of dissertation

This study is divided into five parts. Chapter 2 describes the techniques used to measure ultrasonic velocity and derive elastic constants. Chapter 3 describes anisotropy properties for elasticity and permeability. Chapter 4 discusses the static and dynamic modulus and their relations with other properties. Chapter 5 uses mathematical model to estimate the mechanical properties of shale, and Chapter 6 gives the conclusions and discussion of this dissertation.

Chapter 2 Shale Elasticity Determination from Ultrasonic Velocity Measurement

2.1 Introduction

Shale is generally treated as transverse isotropic porous medium. Many studies have focused on elastic properties and velocity anisotropy of shales (Vernik and Liu 1997, Wang 2002 and etc.). A transverse isotropic rock has a hexagonal symmetry with five independent elastic constants (Love, 1927), which can be derived from velocity measurements. The symmetry axis of isotropy is perpendicular to the bedding planes (Figure 2-1).

(a)

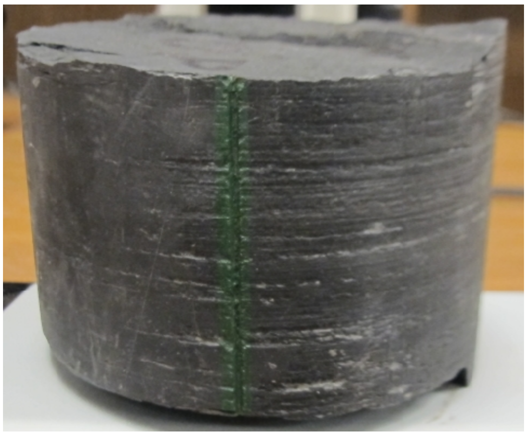

(b)

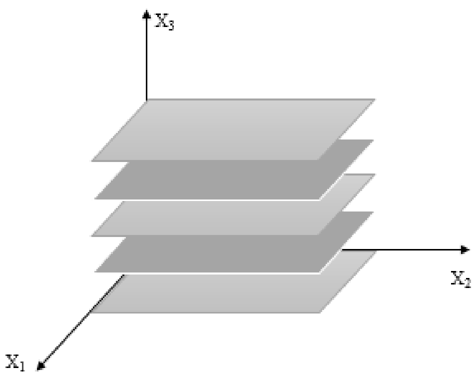

Figure 2-1: (a) Barnett shale core (4 inch in diameter) from Fort Worth Basin. The bedding planes can be seen clearly and symmetry axis vertical to bedding planes. (b) The transversely isotropic medium with vertical symmetry axis (VTI medium), x_3 is the symmetry axis and x_1x_2 plane is isotropic plane.

For a VTI medium shown in Figure 2-1, the stress and strain relationship can be represented as,

$$\sigma_i = C_{ij}\varepsilon_j = \begin{bmatrix} \sigma_1 \\ \sigma_2 \\ \sigma_3 \\ \sigma_4 \\ \sigma_5 \\ \sigma_6 \end{bmatrix} = \begin{bmatrix} C_{11} & C_{12} & C_{13} & 0 & 0 & 0 \\ C_{12} & C_{11} & C_{13} & 0 & 0 & 0 \\ C_{13} & C_{13} & C_{33} & 0 & 0 & 0 \\ 0 & 0 & 0 & C_{44} & 0 & 0 \\ 0 & 0 & 0 & 0 & C_{44} & 0 \\ 0 & 0 & 0 & 0 & 0 & C_{66} \end{bmatrix} \begin{bmatrix} \varepsilon_1 \\ \varepsilon_2 \\ \varepsilon_3 \\ \varepsilon_4 \\ \varepsilon_5 \\ \varepsilon_6 \end{bmatrix} \qquad (2\text{-}1)$$

where σ_i and ε_j are the stress and strain components and C_{ij} is the tensor of elastic constants. Although there are six constants in equation (2-1), only five constants are independent because $C_{66} = 1/2(C_{11} - C_{12})$.

The five independent elastic constants can be derived from ultrasonic velocity and density measurements in the laboratory. Traditionally, three adjacent core plugs at different orientations are cut and measured separately (one parallel, one perpendicular, and one 45 degree to the symmetry axis) (Vernik and Nur, 1992). Single-plug method also can be used for deriving the anisotropic elasticity of shale (Wang, 2002), which saves measuring time and is easy for core preparation.

2.2 Three-plug ultrasonic velocity measurements

We used a three-plug technique to measure velocities and derive the five independent elastic constants. Below figure shows the P-wave and S-wave velocities measured and related elastic constants predicted by using the three-plug technique.

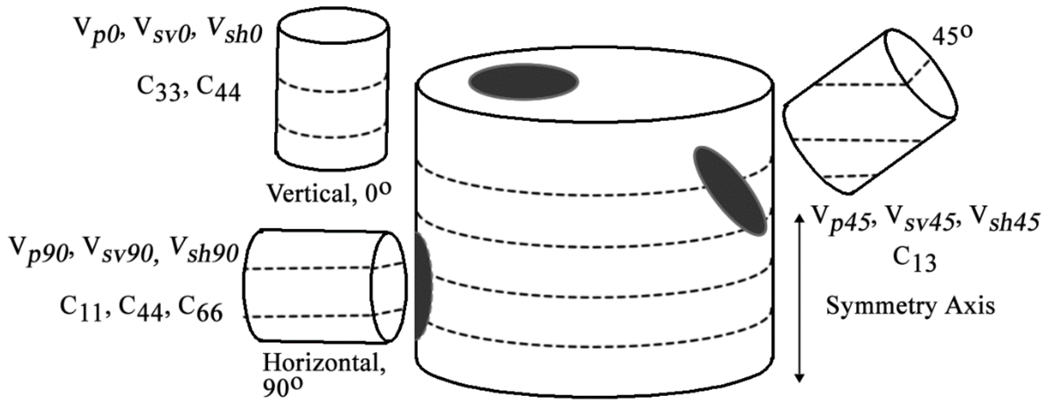

Figure 2-2. Schematic diagram showing the three-plug method for measuring velocity and permeability anisotropy. The dashed lines represent bedding planes. Symmetry axis is normal to bedding planes and five independent elastic constants can be derived from the velocities measured on plugs with different orientation (Lu and Chesnokov, 2015).

Three adjacent one inch diameter plugs (1-2 inch in length) were cut from a four inch diameter core: one vertical, one horizontal, and one 45 degree to the symmetry axis. Figure 2-2 shows in detail how we prepared core plugs and the velocities we measured for each plug. Ultrasonic pulse method was used to measure the travel time of propagating waves and the velocities were measured at the atmospheric conditions (measurement setup shown in Figure 2-3). The phase velocities Vp, Vsh, and Vsv were measured for the three plugs in the directions of 0^o, 45^o, and 90^o relative to the symmetry axis of sample. The velocity we measured was the phase velocity because the size of core plugs were comparable with the size of transducers we used (shown in Figure 2-3, (C) and (D)). According to Dellinger and Vernik (1994), "*Group velocities are very difficult to measure directly; the ratio of core-sample height to transducer width needs to be at least 20, preferably even larger.*"

2.3 Core preparation and phase velocity measurement

The Barnett Shale cores were drilled from wells and shipped to our lab. The original cores were covered by wax to prevent drying. Core plugs were cut cylindrically from carefully selected regions of the core samples by using one inch diamond bit and gasoline as a cooling fluid. Core plugs with one inch to two inches lengths were oriented parallel, perpendicular, and 45 degree to bedding (assuming that shale has transversely isotropic symmetry and bedding plane is the plane of symmetry). Different orientations are essential for evaluating the anisotropic properties of elastic velocity and permeability. After plugging, the two ends of a core plug were ground flat and parallel to each other within 0.05 mm, an important step which helps ensure that the ultrasonic velocity was accurately measured and the pressure can be evenly applied on both ends of the sample. Core plugs were then cleaned in a Soxhlet extraction apparatus with boiling toluene to remove the drilling fluid contaminants. After that, all plugs were heated in a vacuum oven at 100 ^{o}C for 5-8 hours to remove free water. The vacuum level was about 0.08 MPa. All plugs were removed from the oven and allowed to cool for at least 30 min in a desiccator before any experiment were run. The density of each plug comes from the results of the weight and bulk volume measurement. The weight of the plugs is measured by using a digital balance with accuracy of 0.001g and the bulk volume was calculated from their dimensions. The accuracy for density measurement was 0.01g/cm^3.

The digital oscilloscope to record the waveforms was set to a sampling rate of 50

MHz and the first arrival picking time can be made within an uncertainty bound of $\pm$ 20 ns. The central frequency of P-waves and S-waves piezoelectric transducers was 1 MHz. The maximum errors in ultrasonic velocity measurements were 1% for P-wave and about 2% for S-waves depend on the polarization of shear waves.

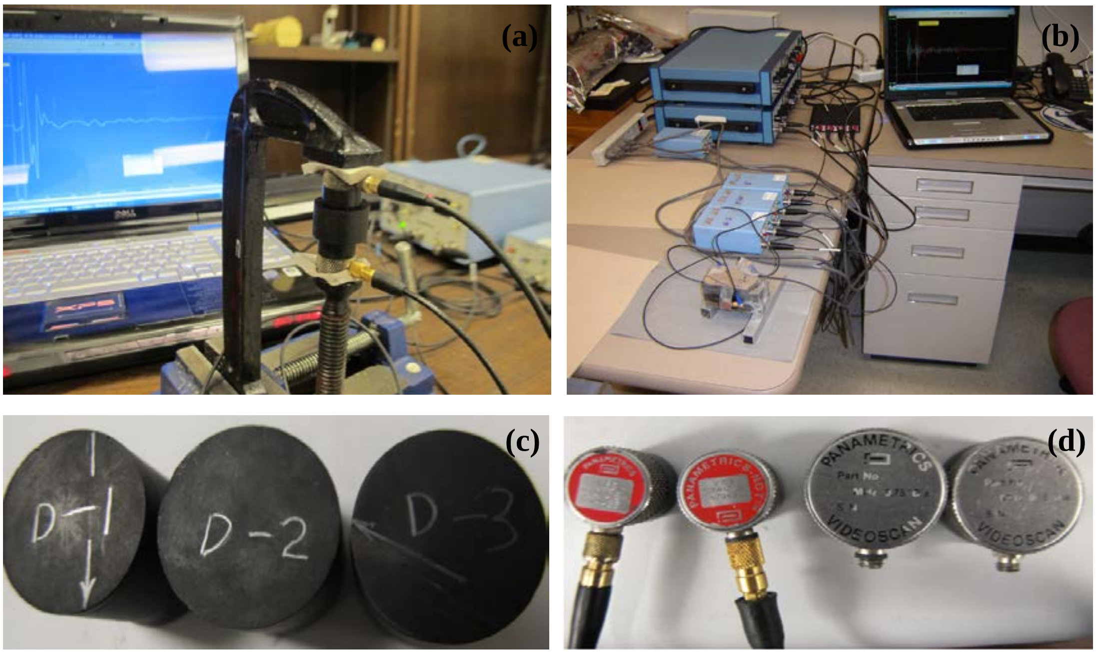

Figure 2-3. (a) Experiment setup at room condition. (b) Photo of the ultrasonic velocity measurement system (from Dyaur et al., 2008). (c) Cylindrical core plugs are cut from three directions, normal to the bedding, parallel to bedding and diagonal at 45 degree to symmetry axis. (d) P-wave (left) and S-wave (right) piezoelectric transducers with central frequency of 1MHz.

In a media with hexagonal symmetry, five independent elastic constants can be obtained by wave propagation related to the plane of isotropy (the bedding planes). The phase velocities in a transversely isotropic medium are given by (Mavko, et al., 1998),

$$2\rho V_p^2 = C_{44} + C_{11}\sin^2\theta + C_{33}\cos^2\theta + \sqrt{(C_{44} + C_{11}\sin^2\theta + C_{33}\cos^2\theta)^2 - 4A} \tag{2-2}$$

$$2\rho V_{sv}^2 = C_{44} + C_{11}\sin^2\theta + C_{33}\cos^2\theta - \sqrt{(C_{44} + C_{11}\sin^2\theta + C_{33}\cos^2\theta)^2 - 4A} \tag{2-3}$$

$$\rho V_{sh}^2 = C_{44}\cos^2\theta + C_{66}\sin^2\theta \tag{2-4}$$

where

$$A = (C_{11}\sin^2\theta + C_{44}\cos^2\theta)(C_{44}\sin^2\theta + C_{33}\cos^2\theta) - (C_{13} + C_{44})^2\sin^2\theta\cos^2\theta$$

and θ is the angle to the symmetry axis.

While the elastic constants are given by the velocity measurements,

$$C_{11} = \rho V_{p,(90^o)}^2 \quad (2\text{-}5)$$

$$C_{33} = \rho V_{p,(0^o)}^2 \quad (2\text{-}6)$$

$$C_{44} = \rho V_{sv,(90^o)}^2 \quad (2\text{-}7)$$

$$C_{66} = \rho V_{sh,(90^o)}^2 \quad (2\text{-}8)$$

For VTI medium, the accuracy of C_{44} can be controlled by Vsv measured on zero degree plug, Vsv(0^o) = Vsv(90^o). While the two shear waves should equal to each other in isotropic planes, Vsh(0^o) = Vsv(0^o). The elastic constant, C_{13}, is usually derived from the velocity measurement from the 45 degree plug (Mavko, et al., 1998),

$$C_{13} = -C_{44} + \sqrt{4\rho^2 V_{P,(45^o)}^4 - 2\rho V_{P,(45^o)}^2 (C_{11} + C_{33} + 2C_{44}) + (C_{11} + C_{44})(C_{33} + C_{44})} \quad (2\text{-}9)$$

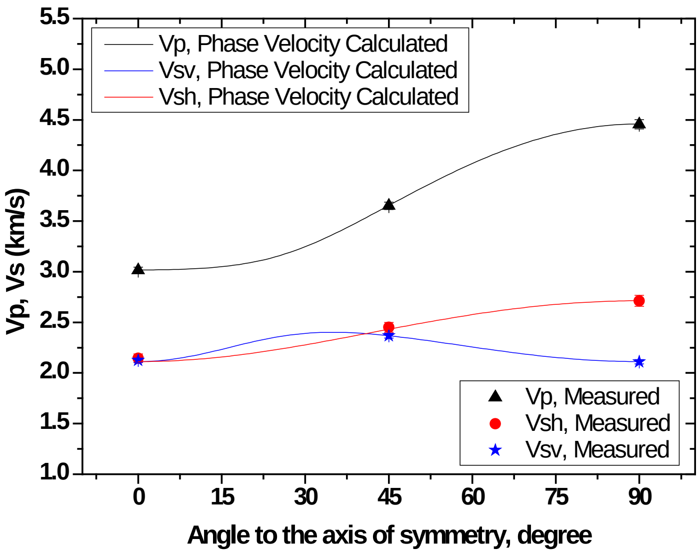

Figure 2-4. The velocity variation of Vp, Vsh, and Vsv with the change of angle of oriented core plugs and the phase velocity curves plotted from the measurements.

The behavior of velocity variation with oriented core plugs (0, 45, and 90 degrees to the symmetry axis) are plotted in Figure 2-4. Phase velocity Vp, Vsh, and Vsv were calculated and plotted according to equations 2-2 to 2-4. The anisotropy behavior shows that the two S-waves Vsh and Vsv propagating through the vertical plug have the same values. The S-wave Vsv, measured on vertical plug, equals that measured on the horizontal plug.

2.4 New method of determining C_{13}

The elastic constant, C_{13}, was determined by the measurements at 45 degree to the symmetry axis. Compressional wave Vp at 45 degree is usually used because of the relatively low error bar of P-wave measurements compare with S-wave measurements.

However, C_{13} is very sensitive to angle error, over 50% error can be caused from an angle error of 5 degree (Yan et al., 2012). The angle is hard to control when cutting 45 degree core plugs, 5 degree angle error is not rare. To solve this problem, we proposed a new method to calibrate the angle error and then estimate C_{13} by using both Vp and Vsv at the real measuring angle.

Traditionally, the elastic constant C_{13} is calculated from the P-wave velocity measured at 45 degree plug by using equation 2-9. However, taking the phase velocity equations 2-2 to 2-4 into consideration, it also can be derived from the velocity Vsv or the combination of Vp and Vsv measured at 45 degree,

$$C_{13} = -C_{44} + \sqrt{4\rho^2 V_{sv,(45^o)}^4 - 2\rho V_{sv,(45^o)}^2 (C_{11} + C_{33} + 2C_{44}) + (C_{11} + C_{44})(C_{33} + C_{44})} \tag{2-10}$$

$$C_{13} = -C_{44} + \sqrt{(\rho V_{p,(45^o)}^2 - \rho V_{sv,(45^o)}^2)^2 - (C_{44} + \frac{1}{2}C_{11} + \frac{1}{2}C_{33})^2 + (C_{11} + C_{44})(C_{33} + C_{44})} \tag{2-11}$$

Therefore, if we assume the cutting angle is correct at 45 degree, we can calculate C_{13} three ways based on equations 2-9, 2-10, and 2-11, shown in Figure 2-5. The difference between these three methods comes from the error of P- and S-wave velocity measurements, angle error for 45 degree, and the heterogeneity of the shale samples.

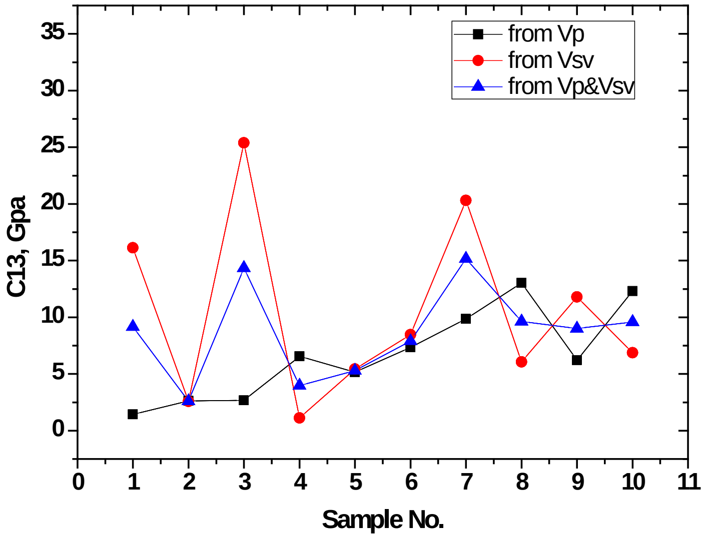

Figure 2-5: Three different ways to calculate C_{13} before measuring angle calibration for the Barnett shale samples.

As we know, cutting angle θ is critical for the accuracy of C_{13} calculation, but it's hard to control the angle in the real measurements, compared with 0 or 90 degree. For VTI medium, we can calculate C_{13} and correspondent angle θ by using expressions 2-2 to 2-4.

Angle θ derived from equation 2-4 can be expressed as,

$$\theta = \arcsin\left(\sqrt{\frac{\rho V_{sh,(\theta)}^2 - C_{44}}{C_{66} - C_{44}}}\right) \tag{2-12}$$

In order to calculate θ, below requirements need to be met,

$$\rho V_{sh,(\theta)}^2 > C_{44} \text{ and } C_{66} > C_{44} \tag{2-13}$$

Also, we can derive the angle θ by using equation (2-2) and (2-3). Namely, adding equation (2-2) to (2-3) leads to the equality,

$$\rho(V_{p,(\theta)}^2 + V_{sv,(\theta)}^2) - (C_{33} + C_{44}) = (C_{11} - C_{33})\sin^2\theta \tag{2-14}$$

And finally,

$$\theta = \arcsin\left(\sqrt{\frac{\rho(V_{p,(\theta)}^2 + V_{sv,(\theta)}^2) - (C_{33} + C_{44})}{C_{11} - C_{33}}}\right) \tag{2-15}$$

In order to calculate θ, below requirements need to be met,

$$\rho V_{sh,(\theta)}^2 > C_{44} \text{ and } C_{66} > C_{44} \tag{2-16}$$

With the real cutting angle θ derived from above equations and the velocities Vp, Vsv, and Vsh measured at that angle, C_{13} can be calculated by substituting θ into (2-2) and (2-3), to obtain the general expressions for estimating of C_{13} at any direction not normal or horizontal to the symmetry axis as,

$$C_{13} \sin\theta\cos\theta = -C_{44} \sin\theta\cos\theta + \sqrt{K - \rho V_{p,(\theta)}^2 F + \rho^2 V_{p,(\theta)}^4} \tag{2-17}$$

$$C_{13} \sin\theta\cos\theta = -C_{44} \sin\theta\cos\theta + \sqrt{K - \rho V_{sv,(\theta)}^2 F + \rho^2 V_{sv,(\theta)}^4} \tag{2-18}$$

$$C_{13} \sin\theta\cos\theta = -C_{44} \sin\theta\cos\theta + \frac{1}{2}\sqrt{4K - F^2 + (\rho V_{p,(\theta)}^2 - \rho V_{sv,(\theta)}^2)^2} \tag{2-19}$$

Where,

$$K = (C_{11} \sin^2\theta + C_{44} \cos^2\theta)(C_{44} \sin^2\theta + C_{33} \cos^2\theta)$$

$$F = C_{44} + C_{11} \sin^2\theta + C_{33} \cos^2\theta$$

To compare the variations of cutting angle and C_{13} determination, we listed the calculating results by using different methods as seen in Table 2-1. The results show that, C_{13} estimated from the three methods (2-17 to 2-19) becomes equal only when θ was determined by equation 2-15.

Table 2-1: Comparison of different ways of angle calibration and relative C_{13} determination.

Sample	**Angle**		***Vp***	***Vsv***	***Vp&Vsv***
			C_{13}	**C_{13}**	**C_{13}**
No.1	**45**	45.00	2.63	2.57	2.60
	θ_1	47.04	-0.83	2.13	0.71
	θ_2	45.04	2.56	2.56	2.56
No.2	**45**	45.00	3.05	5.08	4.07
	θ_1	42.89	5.41	5.32	5.37
	θ_2	42.98	5.32	5.32	5.32
No.5	**45**	45.00	6.55	1.12	3.98
	θ_1	44.10	7.84	1.38	4.79
	θ_2	48.52	-0.28	-0.28	-0.28
No.7	**45**	45.00	10.17	10.83	10.50
	θ_1	42.89	10.94	10.85	10.90
	θ_2	43.13	10.85	10.85	10.85
No.8	**45**	45.00	11.66	2.60	7.22
	θ_1	43.43	13.37	2.68	8.13
	θ_2	52.36	1.94	1.94	1.94
No.9	**45**	45.00	13.03	6.07	9.65
	θ_1	43.32	15.11	6.26	10.80
	θ_2	50.10	5.21	5.21	5.21
No.10	**45**	45.00	17.01	6.23	11.79
	θ_1	51.01	9.01	6.11	7.58
	θ_2	52.71	6.06	6.06	6.06

Note: θ_1 is the angle calculated from equation 2-12, θ_2 is the angle calculated from equation 2-15 and 45 means we assume the measuring angle is right at 45 degree. C_{13},(Vp), C_{13},(Vsv), and C_{13},(Vp&Vsv) are C_{13} calculated from equations 2-17, 2-18, and 2-19 respectively.

With the general expressions of C_{13} at any angle, we can plot the angle dependence curves (Figure 2-6) by using equations 2-17 to 2-19 as provided above. The angle dependence curves show that: compared with Vsv, Vp is more sensitive to angle changes at the range of ±5 degree around 45 degree, which means the traditional way of using Vp alone to estimate C_{13} is not accurate. For example, this sample gave us about 40% error from a five degree angle error around 45 degree by using Vp. But only 3% error can be caused by five degree angle error around 45 degree by using Vsv. This phenomenon has been observed for all the samples tested.

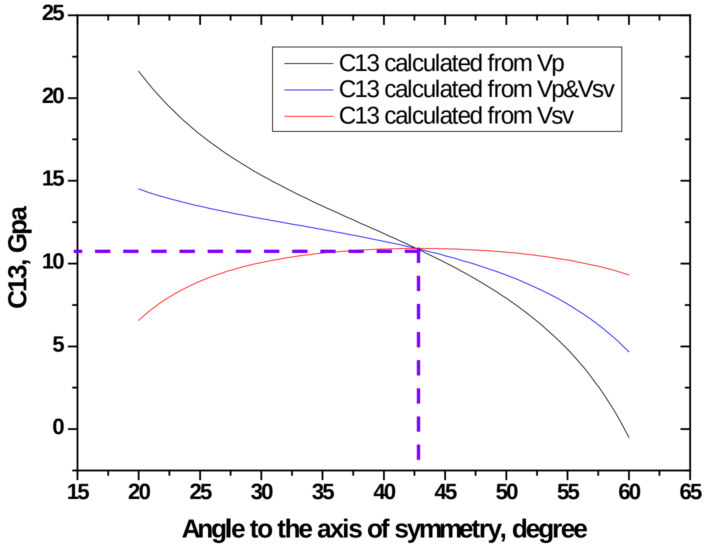

Figure 2-6: Angle dependence curves for determination of C_{13}.

The cross-point of these curves gave us the real measuring angle and C_{13}. Therefore, the equation 2-15 and the general expressions 2-17 to 2-19 can be used to determine the measuring angle and then calculate C_{13} accurately.

2.5 Improvement of permeability tensor measurement by angle calibrating

Permeability of shale has a directional dependency, which can be considered as a second rank tensor (Metwally and Chesnokov, 2010). A modified transient-flow technique was used to measure the permeability of shale samples (Lu et al., 2015). We measured the permeability of three oriented core plugs (vertical, horizontal, and 45 degrees to the symmetry axis) by using the specially designed apparatus (Figure 2-7).

The three core plugs were measured simultaneously under the same conditions of confining pressure, pore pressure, and temperature.

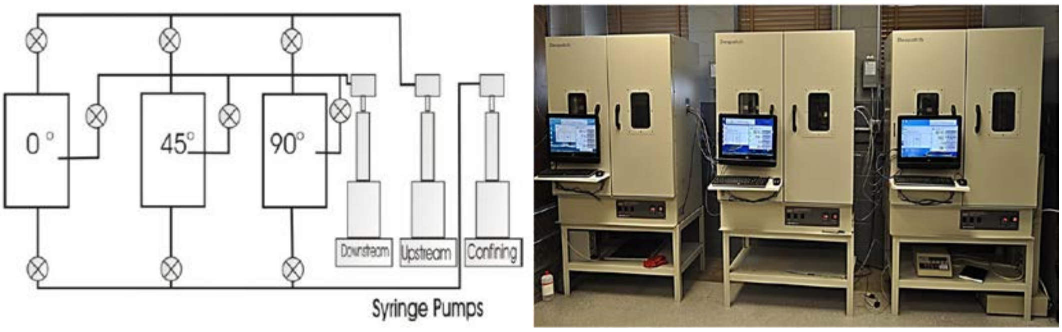

Figure 2-7. (a) Schematic diagram of the specially designed permeability tensor measurement system. It has three hydrostatic pressure vessels and they are controlled by three syringe pumps. (b) Photo of apparatus for permeability tensor measurement system (Metwally and Chesnokov, 2010).

As the permeability measured from 45 degree core plug is also affected by the cutting angle. It's necessary for us to calibrate the cutting angle error in order to improve the accuracy of permeability tensor measurements. Below figure shows the permeability tensor measurement results after 45 degree angle calibration.

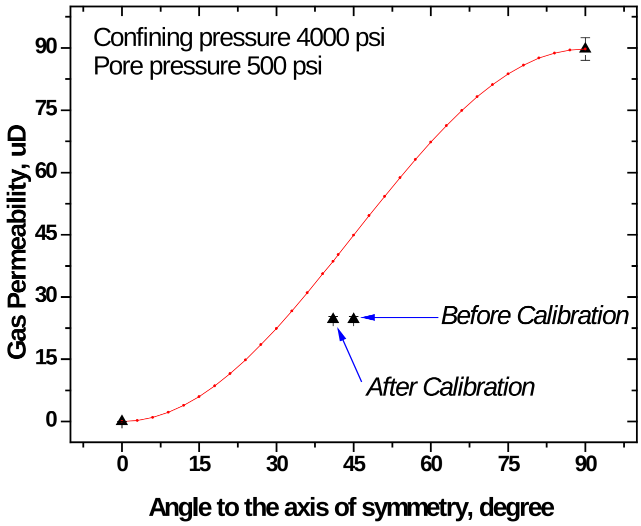

Figure 2-8: Gas permeability measured for three oriented cores with confining pressure of 4000 Psi and pore pressure 500 Psi. After calibration, we can see the substantial improvement of permeability at 45 degree.

2.6 Summary

Our laboratory results reveal that the accuracy of elasticity measurement is quite dependent on the velocity measurement at 45 degree, especially for VTI rocks. We developed a new method of calibrating the cutting angle at 45 degree and estimating the elastic constant C_{13}. Our measurements indicate that using Vp alone to estimate C_{13} is not accurate due to its high-sensitivity to angle error. By considering both Vp and Vsv, we can reduce the error caused by the cutting angle and estimate C_{13} in a more accurate way. By calibrating the cutting angle error, the accuracy of permeability tensor measurements are also improved. Although we used a three-plug method to derive elasticity, this new technique can be applied to both three-plug or single-plug ultrasonic measurements.

Chapter 3 Anisotropic properties of Barnett Shale: Velocity anisotropy and Permeability anisotropy

3.1 Introduction

In recent year, unconventional gas reservoirs like shales have become an important sources for natural gas production. The success of shale gas stimulates the demands for understanding the physical properties of these tight rocks. Anisotropy is a characteristic when the physical parameters have direction dependency. Barnett shale is a clay-rich siliceous rock. The anisotropy of shales have been reported to be caused by mineral orientation (Christensen and Johnston, 1995), crack orientation (Hornby at al., 1994), and the clay and organic materials alignment (Vernik and Nur, 1992; Vernik and Liu, 1997; Sondergeld, 2000; and Vernik and Milovac, 2011). Understanding the causes of anisotropy and correlations between anisotropic velocities are crucial for interpretation of the sonic or seismic data.

The permeability of shale also exhibits high anisotropy. Many authors, Bustin et al (2008), Civan et al (2010a, 2010b), and Metwally and Sondergeld (2011), have been trying to measure shale’s permeability tensor and improve the accuracy of the measurement. However, research focusing on the correlation between elasticity and permeability of shales are scarce. Some literature were trying to link permeability with seismicity. Bayuk and Chesnokov (1998) used the general singular approximation method to estimate permeability from experimental data of elasticity and conductivity.

Goloshubin et al. (2008) used seismic attributes to estimate reservoir permeability. Muller et al. (2010) explored the attenuation and dispersion effects of porous medium to seismic waves. There is a clear need for more effort on shales to understand the relationship between elasticity and flow properties.

.

3.2 Mineral composition – XRD method

The mineralogy composition of shale samples is required for understanding the elastic anisotropy and theoretical modeling of the Barnett shale. X-ray diffraction (XRD) technique is used to estimate the mineralogical assemblages by evaluating the intensity pattern of diffracted X-ray beam from a powdered sample. The weight percentage concentration of each mineral is determined by the intensity of the diffraction peak, which is a function of incident and scattered angle, polarization, and wavelength for the X-ray beam related to internal mineral composition and structure. The XRD results, including mineral types and weight percentages are shown in Table 3-1.

Table 3-1: Mineralogical composition of twelve Barnett Shale samples (core plugs provided by Devon Energy Co.), in weight percentage using XRD method. (Data courtesy of Dr. Yasser M. Metwally)

Sample	**A**	**B**	**C**	**D**	**E**	**F**	**G**	**H**	**I**	**J**	**K**	**L**
Quartz	57	7	60	36	47	66	66	52	71	24	71	71
Feldspar	0	0	1	0	1	0	0	0	0	2	1	0
Albite	4	1	3	4	2	2	3	4	3	4	2	1
Pyrite	3	0	3	3	2	1	1	2	3	1	2	2
Calcite	8	58	9	27	10	2	3	9	0	2	1	2
Dolomite	2	3	1	2	7	4	0	3	1	8	1	1
Aragonite	1	0	2	1	2	1	2	1	1	2	2	3
Siderite	1	0	0	1	1	0	0	1	1	3	1	1
Sulfates & Halite	5	22	5	13	7	2	4	6	1	10	2	1
Total Clays	18	7	15	12	21	21	20	21	16	44	18	16

From XRD results, we can see the common minerals in Barnett shale are quartz, feldspar, carbonates, and clays. Barnett shale is one of siliceous shales with high concentrations on quartz and clay minerals. Figure 3-1 is the ternary plot of mineral composition for all 19 samples provided by Devon or Marathon, which shows 70% of samples have high concentration of quartz, feldspar, and clay contents. Quartz and feldspar contents range from 60% to 80% of weight percentage. Clay content ranges from 20% to 40% of weight percentage. There are several exceptions that about seven samples from the Marathon dataset are dominated by large carbonate crystals. Those are calcareous mudstones drilled from the top and bottom limestone layers where the Barnett lies between.

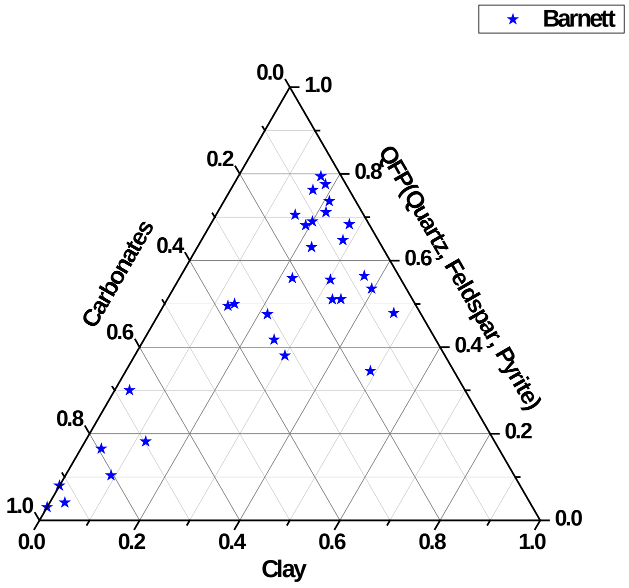

Figure 3-1. Ternary plot of the Barnett sample composition. Most Barnett samples show high quartz and relative high clay concentrations. Several samples show high carbonate concentrations, which are calcareous mudstones at the top or bottom of shale layer.

3.3 Microstructure

The microstructure analyses are mainly used to give qualitative information about mineral orientation, organic matter distribution, and aspect ratio. The aspect ratio, α, defined as the short axis divided by the long axis can help to constrain the mathematical modeling and thus reach more accurate results. Scanning electron microscope (SEM) and focused ion beam (FIB) are electron microscope that produces images of a sample by scanning it with a focused beam of electrons or ions. Microphotograph of some representative samples used in this study are shown in Figure 3-2 and Figure 3-3.

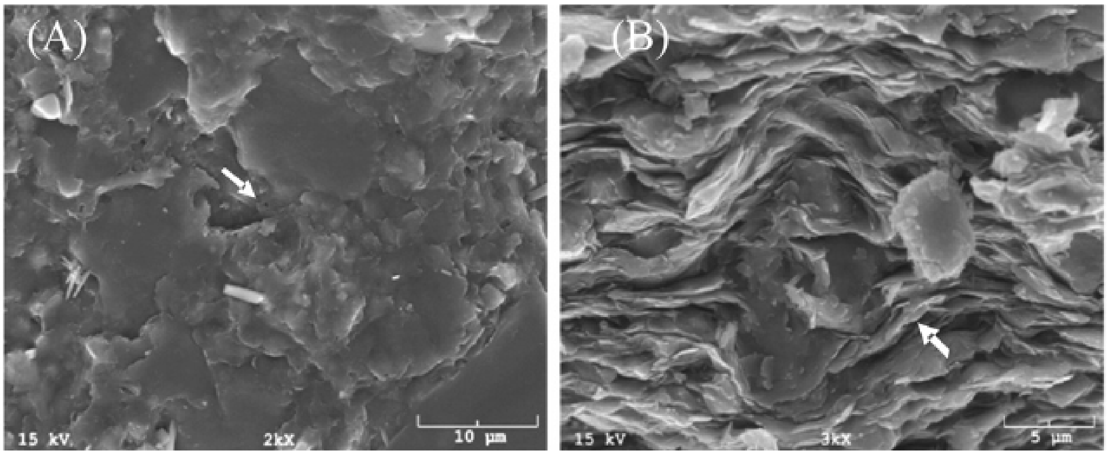

Figure 3-2. SEM microphotograph. (A) micro-structure of shale layers formed by mineral (clay particles) alignment with a view normal to the bedding planes. Small pores can be seen between planes. (B) micro-structure of shale layers formed by mineral (clay particles) alignment with a view parallel to the bedding planes. Large quartz and other rigid mineral can be seen between layers. Connected flowing channels are built along these layers (Metwally and Sondergeld, 2011).

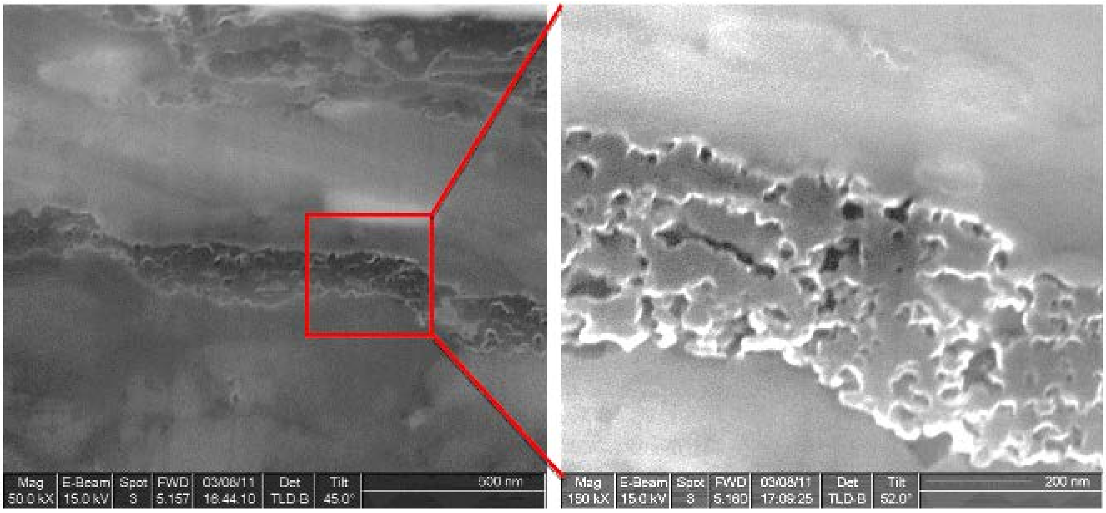

Figure 3-3. FIB microphotograph show the alignment of organic content with a view normal to the bedding planes. Small pores are oriented in the organic matter layers. (Di, Master Thesis, 2012).

The typical microstructures of Barnett shale was exhibited in Figure 3-2. In the normal-to-bedding direction (image A), sheet-like fabrics were constructed by some platy-shaped minerals such as clay and mica. Rounded and sub-rounded porosities (aspect ratio, $\alpha \sim 0.5$–1) can be seen within these platy fabrics. In the parallel-to-bedding direction (image B), the bedding planes were defined by the preferred orientations of matrix clay. The parallel planes were twisted at some positions by the relatively harder minerals like quartz, feldspar, calcite, or dolomite, which may reduce the anisotropy of shale (Metwally and Sondergeld, 2011). Pores appear as thin layers ($\alpha < 0.05$) can be seen along these bedding planes.

Figure 3-3 shows the common distribution of organic matters in Barnett shale. Shapes of pores in organic matters vary from nearly rounded to thin cracks. The alignment of organic matters and cracks included become a strong source of shale anisotropy. Previous studies have reported the anisotropic causes related to organic contents in the rock (Vernik and Nur, 1992; Vernik and Liu, 1997).

3.4 Anisotropy parameters and relation to mineral composition

For a VTI medium, shales have five independent elastic constants which can be derived from velocities and densities measured in laboratory. With elastic constants, the Thomsen P- and S- wave anisotropy parameters (Thomsen, 1986) ε, γ, and δ can be calculated as,

$$\varepsilon = \frac{C_{11} - C_{33}}{2C_{33}} \tag{3-1}$$

$$\gamma = \frac{C_{66} - C_{44}}{2C_{44}} \tag{3-2}$$

$$\delta = \frac{2(C_{13} + C_{44})^2 - (C_{33} - C_{44})(C_{11} + C_{33} - 2C_{44})}{2C_{33}^2} \tag{3-3}$$

We cross plot the anisotropy parameters ε and γ in Figure 3-4. Our laboratory results (room condition) are compared with core data (10 MP confining pressure) from Marathon dataset. Based on the measurement results, Barnett shale exhibits a large variety of anisotropy. Anisotropy ranges from 5% to 73% for P-wave parameter ε and 7% to 47% for S-wave parameter γ. Several samples show a very high anisotropy. The results with confining stress (red dots, Marathon dataset) have a good linear correlation between ε and γ. While the unconfined results (blue points, cores from Devon Energy Co.) show a scatting pattern for P- and S-wave anisotropy correlation, which may indicate that fractures or cracks developed in core samples under unconfined status will change the anisotropic properties of shale.

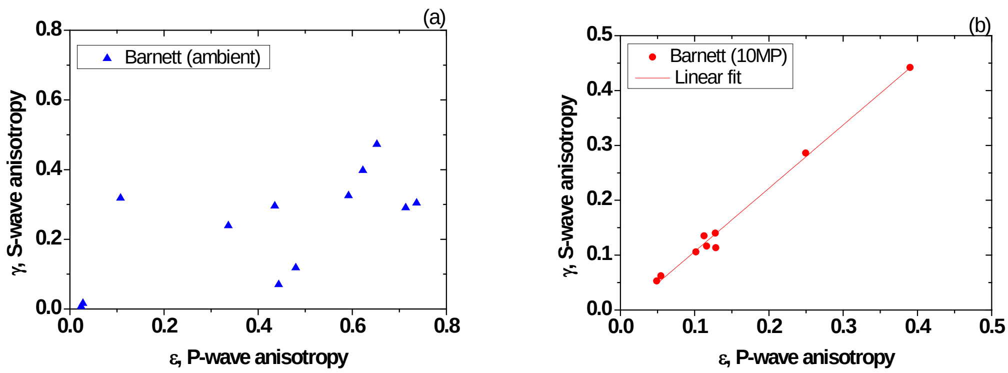

Figure 3-4. Relation between P wave and S wave Thomsen anisotropy parameter. (a) Velocity anisotropy measured under room condition. (b) Velocity anisotropy measured under 10 MP pressure condition.

Correlation between Thomsen P- and S- wave anisotropy parameters ε and γ and other rock properties have been reported (Tsuneyama and Mavko (2005), Li (2006), Sone and Zoback (2013)). In order to understand what factors control the mechanical anisotropy of Barnett shale, we cross plot the Thomsen anisotropy parameter with the clay and total organic content (TOC).

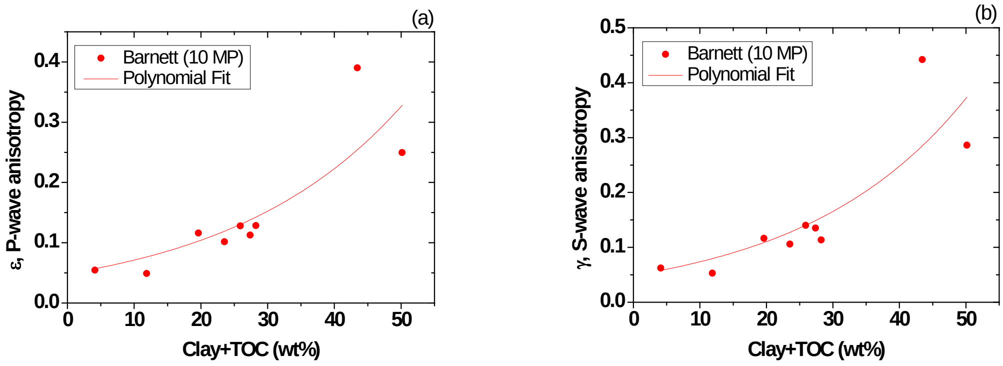

Figure 3-5. (a) Relation between Thomsen P-wave anisotropy parameter and clay plus TOC contents. (b) Relation between Thomsen S-wave anisotropy parameter and clay plus TOC.

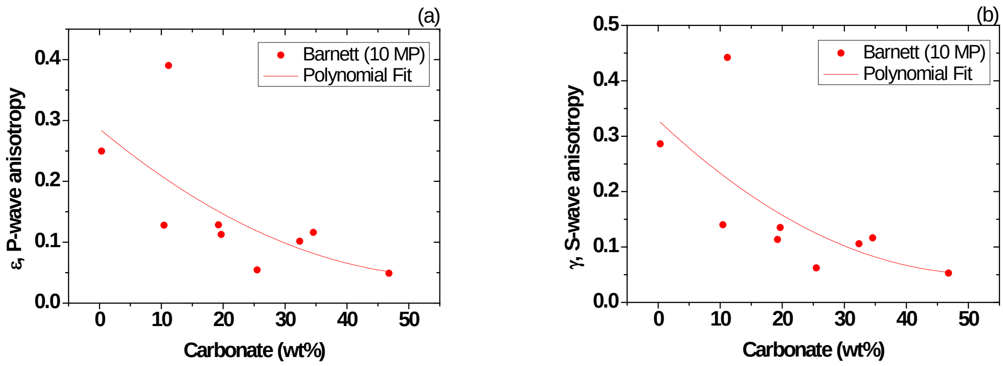

Figure 3-6. (a) Relation between Thomsen P-wave anisotropy parameter ε and carbonate contents. (b) Relation between Thomsen S-wave anisotropy parameter γ and carbonate contents.

Figure 3-5 and Figure 3-6 shows the effect of mineral composition, clay and TOC, and carbonate contents on shale's elastic anisotropy. The percentage of elastic anisotropy increases with the increase of clay and TOC contents, while it decreases with the increase of carbonate contents. These effects meet our expectation because when carbonate increased, the rocks become more isotropic like mudstone or limestone. When clay increased, the rocks tend to exhibit laminar structure which causes the anisotropy physically. Other properties like porosity, quartz, and feldspar contents have also been cross plotted with the Thomsen anisotropic parameters, no clear relations have been observed.

3.5 Vp – Vs relation

Several authors have reported the Vp-Vs relations for different types of sedimentary rocks. Castagna et al. (1985), Castagna et al. (1993A) pointed out the empirical relation between P-wave and S-wave velocities for common sandstone. Vernik and Liu (1997) investigated the Vp-Vs relations for shales from different reservoirs. The velocity-data measured in laboratory for the Barnett shale was compared with the other shale data literature (Vernik and Liu, 1997). The constant Vp-Vs ratio lines are plotted to help us understand the ratio variation.

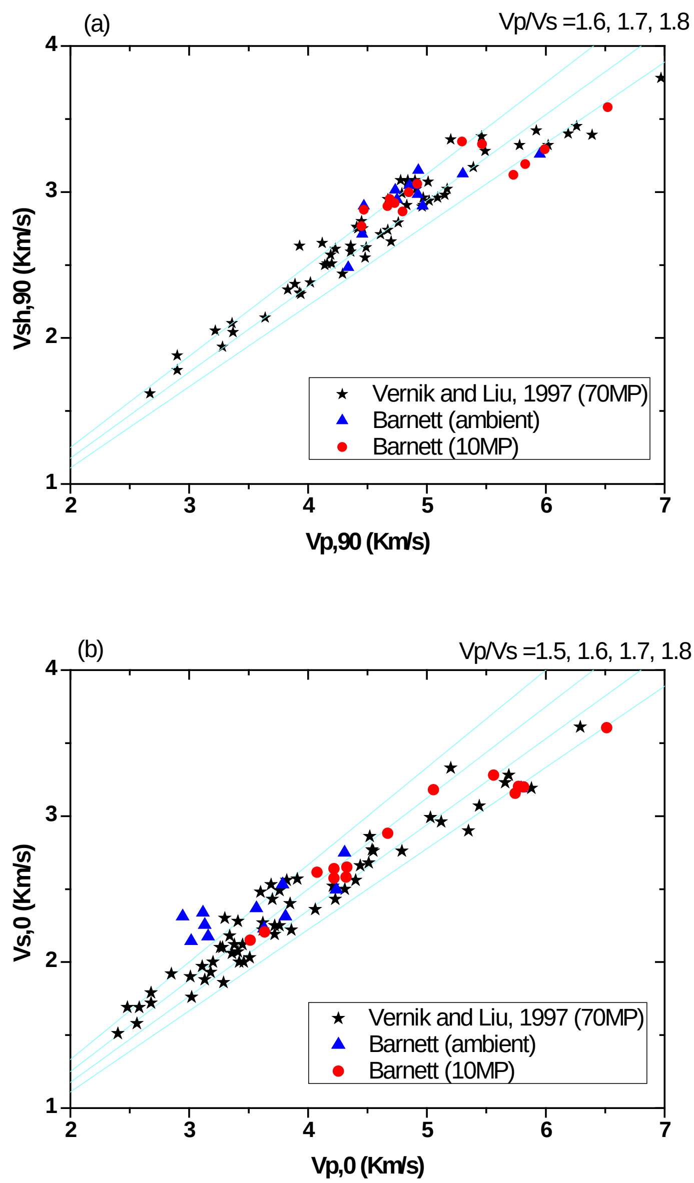

Figure 3-7: (a) Vp-Vs plots for wave propagating along the bedding plane. 'Vp,90' is P-wave velocity horizontal to bedding planes (90 degree to symmetry axis). Vsh was chosen here as S-wave with polarization in the bedding planes. (b) a Vp-Vs plot for wave propagating normal the bedding planes. 'Vp,0' stands for P-wave velocity vertical to bedding planes (0 degree to symmetry axis).

In this section, we plot the Vp-Vs relations at vertical and horizontal directions to bedding planes. Note that the velocity data from Vernik and Liu (1997) were measured under 70 MPa confining pressure. It is not surprisingly that different shales has different empirical Vp-Vs relations due to various concentrations on minerals and organic matters. We represent both vertical and horizontal velocity of the VTI medium in Figure 3-7. In general, we have narrow range of Vp/Vs ratio from 1.6 to 1.8 at horizontal to beddings direction and a relatively large range of Vp/Vs ratio from 1.5 to 1.8 at vertical to beddings direction. Although the Vp/Vs ratio may vary with the sample preparations and the measurement conditions in laboratory, this relation for shales will help to predict shear-wave velocity in case of absence of shear-velocity data in field.

3.6 Relation between vertical and horizontal velocity

For VTI medium like shale, both vertical and horizontal velocity are essential to understand the anisotropic properties. However, in most cases, only vertical velocity can be expected in the well log data. The relation between vertical and horizontal velocity are useful to interpret the anisotropic properties of reservoir especially for shale plays.

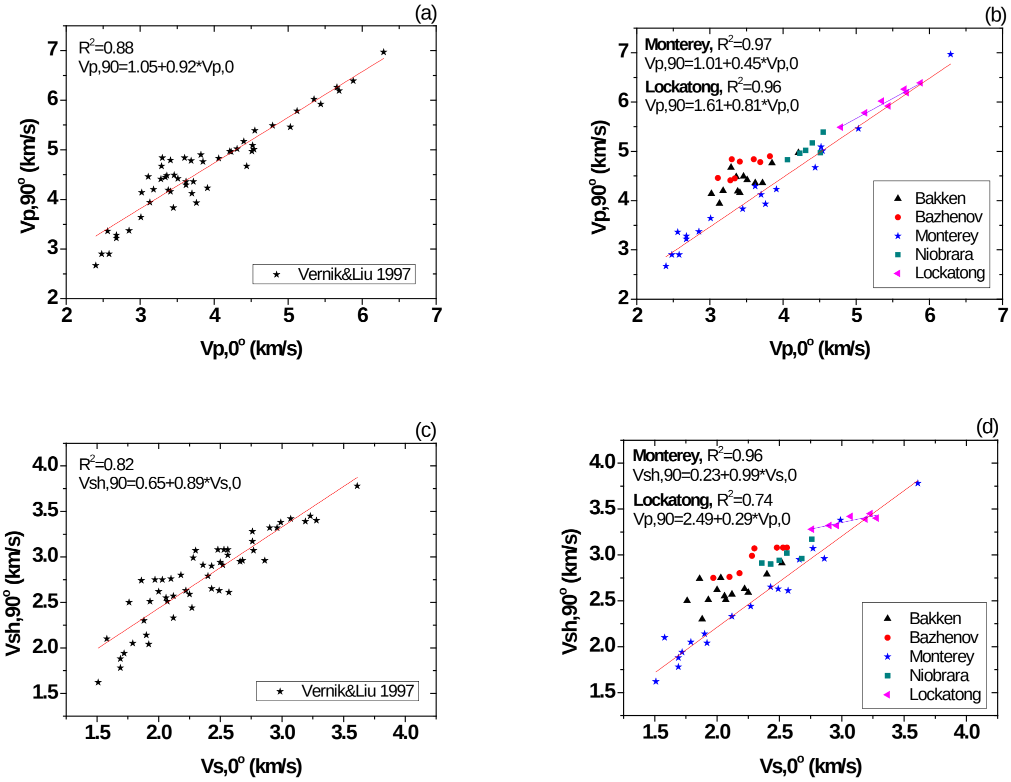

Figure 3-8: Vertical and horizontal velocity interpretation for data from Vernik and Liu (1997). (a) Vertical Vp vs. horizontal Vp for all shales. (b) Vertical Vp vs. horizontal Vp for specific type of shales. (c) Vertical Vs vs. horizontal Vs for all shales. (d) Vertical Vs vs. horizontal Vs for specific type of shales. In this plot, Vsh was chosen as S-wave propagating along the bedding planes.

Figure 3-8 shows the correlation between vertical velocities and horizontal velocities based on data from Vernik and Liu (1997). As the shale samples in Vernik and Liu (1997) included several different shale plays, we also plotted some good correlations for specific shale plays. Note that not all shale plays show good relation between vertical and horizontal velocities, which can be explained as the mean of anisotropy varying from reservoir to reservoir. However, it’s still helpful to predict the elastic anisotropic properties in the field if close correlation can be found from lab measurements.

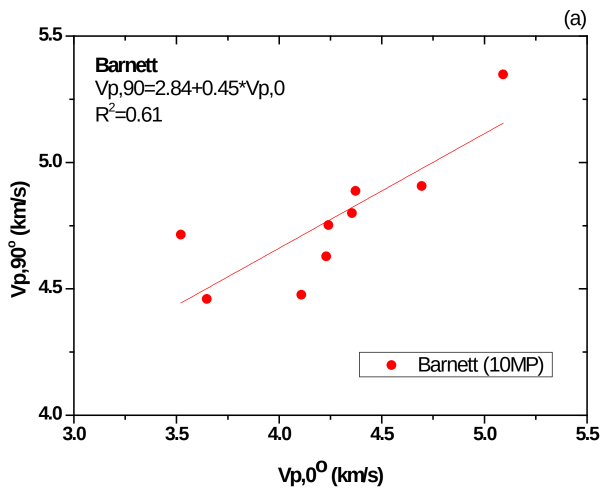

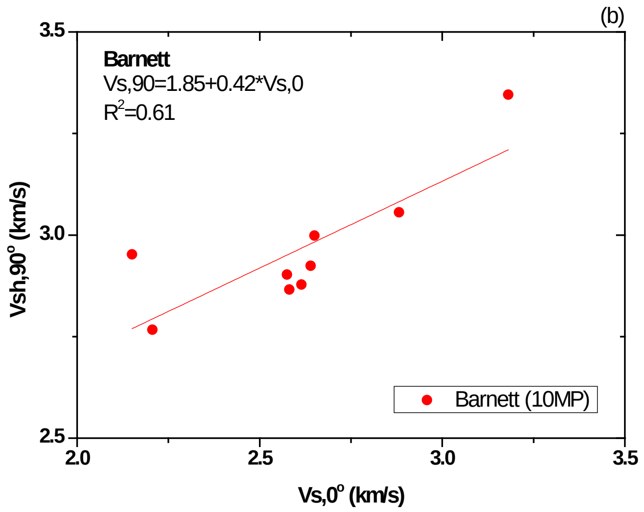

Figure 3-9: (a) Vertical Vp vs. horizontal Vp for Barnett shale. (b) Vertical Vs vs. horizontal Vsh for Barnett shale shales. Vsh was chosen as S-wave with polarization in the bedding planes.

We plot correlation of vertical velocities and horizontal velocities for Barnett shale in Figure 3-9. Although our Barnett shale data is still limited, we derived empirical relations between the vertical and the horizontal velocity for both P- and S-waves. The empirical relations for Barnett shale are,

$$V_{p,90} = 2.84 + 0.45 \times V_{p,0} \tag{3-4}$$

$$V_{s,90} = 1.85 + 0.427 \times V_{s,0} \tag{3-5}$$

3.7 Relation between permeability anisotropy and velocity anisotropy

Permeability of shale has a directional dependency, which can be considered as a second rank tensor (Metwally and Chesnokov, 2010). Permeability tensor can be measured accurately in the laboratory. Although the wave propagation and fluid flow are two different physical processes, they are be related through the porous medium. The fluid flow can cause attenuation and dispersion of elastic waves (Muller et al., 2010). Therefore, studying the relationship between elastic wave anisotropy and permeability anisotropy has the potential to estimate permeability. If the correlation between them can be built, we can predict the formation permeability from the surface seismic data. In this section, we measured elastic anisotropy and permeability anisotropy for the same VTI rocks and compared the results in below figures.

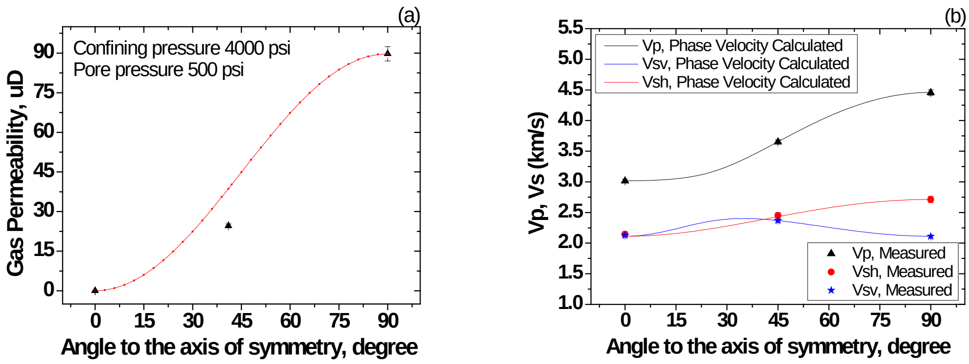

Figure 3-10: (a) Gas permeability tensor measured under confining pressure of 4000 Psi and pore pressure 500 Psi. (b) Velocity variation of Vp, Vsh, and Vsv with the change of angle of oriented core plugs and the phase velocity curves plotted from the measurements.

Figure 3-10(a) shows the permeability anisotropy behavior of one shale sample. The permeability parallel to bedding planes is about 90 uD (micro Darcy) while the permeability normal to the bedding planes falls to the nano Darcy scale. The permeability parallel to the bedding planes is at least two orders lager in magnitude than that normal to the bedding planes. It demonstrates that the dominant flow for a shale formation is the fluid flow parallel to the bedding planes. Compared with Figure 3-10(b), the permeability and velocity anisotropy are closely related along the symmetry axis. Both P-wave velocity and permeability reach to the highest value at the direction parallel to bedding planes.

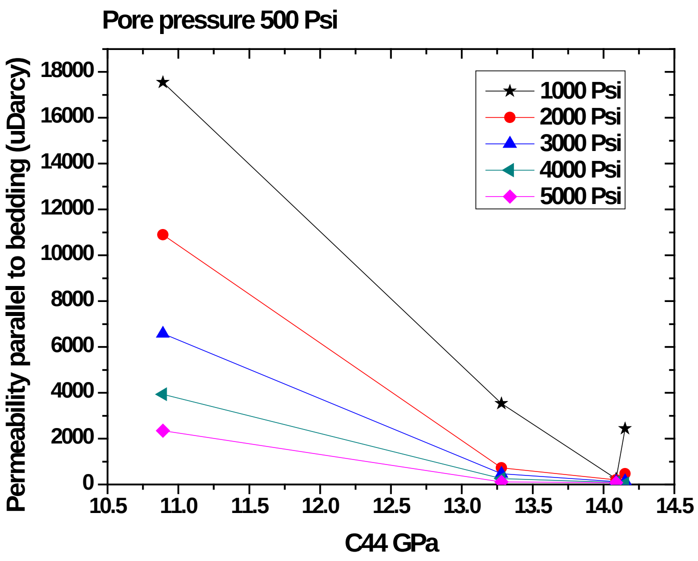

Figure 3-11. Correlation between permeability parallel to bedding plane and elastic constant C44 (Lu et al., 2015).

The relationship between permeability and elastic constant C44 is cross-plotted in Figure 3-11. Permeability parallel to bedding planes shows a decreasing trend with the increasing of C44, which is derived from Vsv (the S-wave velocities polarized normal to the bedding plane). From this empirical relations, we believe that the S-wave can be used to estimating permeability qualitatively for VTI rocks like shale. However, more statistical studies are needed to validate these observations.

3.8 Summary

Wide variation in elastic properties of shale are observed from obtained data. Permeability anisotropy is much more sensitive than velocity anisotropy. Permeability along bedding planes could be two orders of magnitude larger than that vertical to bedding planes. Thomsen anisotropy parameters was found to be correlated with clay and organic content. Compared with confined measurements, an unconfined shale sample display higher anisotropy and more scattering in Thomsen anisotropy parameters.

The trend of Vp/Vs ratio for Barnett is consistent with other shales experimental data (Vernik and Liu, 1997). Besides, close correlations were found between the vertical and horizontal velocities for different shale plays. Because of the wide variation of elastic properties from reservoir to reservoir, empirical relations were suggested for specific shale plays including Barnett shale.

Our results show that permeability anisotropy and velocity anisotropy have good correlation behaviors along the symmetry directions. The highest permeability and highest velocity can be expected along bedding planes. Correlation between dominant permeability (parallel to bedding plane) and elastic constant C_{44} has been identified. To verify these observations, more statistical studies need to be conducted, especially on the simultaneous measuring elasticity and permeability under the same conditions.

Chapter 4 Dynamic and Static Moduli of Barnett Shale

4.1 Introduction

Mechanical properties of rocks, such as Young's modulus and Poisson's ratio, are useful in estimating the in-situ stress and designing hydraulic fractures especially for unconventional reservoirs with low permeability. The elastic parameters are essential to estimate the Young's modulus and Poisson's ratio. In industry, the mechanical properties are still estimated by assuming isotropic formation which is applicable for sandstone reservoirs. But for shale, in presence of bedding planes, strong anisotropy of shale formation should be considered. Chesnokov et al. (2010) discussed a technique allowing inversion of the shale stiffness tensor with VTI symmetry from standard logging data.

Dynamic and static moduli are two kinds of parameters can be measured from different methods. The dynamic method is calculated from the elastic wave velocity measurement at known frequencies (ultrasonic/sonic/seismic), which is a nondestructive geophysical approach. While the static method is based on the stress and strain response of material in a deformational experiment. It is known that the static moduli are related the brittleness of rocks which is important to the local or reginal zone of interest. Correlation of rock static and dynamic modulus is useful to determine the elasticity and brittleness of rock formation by using acoustic logging or seismic data. In this study, the dynamic and static testing results on Barnett shale cores are provided by Marathon Oil Company.

4.2 Anisotropic Moduli of Single Minerals in shale

The Young's modulus and Poisson's ratio are used to estimate the sweet spots and fracture zones in industry. Low Poisson's ratio and high Young's modulus give good fracture zones (Banik and Egan, 2012). However, these moduli are usually calculated as isotropic cases, which may be true for rock like sandstone. But for rock layers with high anisotropic properties, the mechanical moduli vary in directions of different symmetry axes. For isotropic material, the Young's modulus E and Poisson's ratio ν can be expressed as follows (Marvko, et. al.,1998):

$$E = \frac{9K\mu}{3K + \mu} \tag{4-1}$$

$$\nu = \frac{3K - 2\mu}{2(3K + \mu)} \tag{4-2}$$

where K is the bulk modulus and μ is the shear modulus. The theoretical value of Poisson's ratio for isotropic material ranges from -1 to 0.5 (Thomsen, 1990).

The anisotropic formulae for Young's modulus and Poisson's ratio have been derived and summarized in Table A-1 of Appendix A. For rock layers with anisotropic properties like shale, the anisotropy of mechanical moduli vary at different directions with different symmetry types. Barnett shale is composed of clay and silicate rich minerals, it is essential to know the difference between isotropic estimation and anisotropic estimation for the common minerals in shale.

Table 4-1: Comparison of anisotropic Young's modulus and Poisson's ratios with isotropic formula and anisotropic formula for some common minerals in shale.

<table>
<tr><th rowspan="2">Mineral</th><th rowspan="2">Sym.</th><th colspan="2">Isotropic</th><th colspan="9">Anisotropic</th></tr>
<tr><th>E</th><th>υ</th><th>E11</th><th>E22</th><th>E33</th><th>υ12</th><th>υ21</th><th>υ13</th><th>υ23</th><th>υ31</th><th>υ32</th></tr>
<tr><td></td><td></td><td>Gpa</td><td></td><td>Gpa</td><td>Gpa</td><td>Gpa</td><td></td><td></td><td></td><td></td><td></td><td></td></tr>
<tr><td>Pyrite</td><td>cubic</td><td>296.7</td><td>0.15</td><td colspan="3">355.3</td><td colspan="6">0.09</td></tr>
<tr><td>Halite</td><td>cubic</td><td>36.9</td><td>0.26</td><td colspan="3">42.9</td><td colspan="6">0.22</td></tr>
<tr><td>Illite</td><td>Hex.</td><td>102.1</td><td>0.22</td><td colspan="2">168.7</td><td>53.1</td><td colspan="2">0.2</td><td colspan="2">0.21</td><td colspan="2">0.07</td></tr>
<tr><td>Kaolinite</td><td>Hex.</td><td>98.1</td><td>0.25</td><td colspan="2">153.6</td><td>45.6</td><td colspan="2">0.16</td><td colspan="2">0.43</td><td colspan="2">0.13</td></tr>
<tr><td>Chlorite</td><td>Hex.</td><td>181.8</td><td>0.26</td><td colspan="2">162.2</td><td>103.3</td><td colspan="2">0.3</td><td colspan="2">0.13</td><td colspan="2">0.09</td></tr>
<tr><td>Apatite</td><td>Hex.</td><td>120.6</td><td>0.26</td><td colspan="2">112</td><td>117.8</td><td colspan="2">-0.12</td><td colspan="2">0.43</td><td colspan="2">0.45</td></tr>
<tr><td>Aragonite</td><td>Ortho.</td><td>94.4</td><td>0.17</td><td>143.7</td><td>75.7</td><td>81.8</td><td>0.44</td><td>0.23</td><td>-0.06</td><td>0.18</td><td>-0.03</td><td>0.19</td></tr>
</table>

Notes: 'Sym.' is abbreviation of symmetry type. For symmetry type, 'Hex.' and 'Ortho.' stand for hexagonal and orthorhombic symmetry. The elastic constants for each mineral come from several references (refer to Table 5-1 and Table 5-2).

Table 4-1 exhibits the difference between averaged 'isotropic' and real anisotropic calculations of Young's modulus and Poisson's ratio. In averaged 'isotropic' case, values are calculated by using equation 4-1 and 4-2 with the bulk modulus and shear modulus of minerals. We want to point out that cubic mineral shows a behavior similar to isotropy, $E_{11}=E_{22}=E_{33}$, just because cubic symmetry attains same values along the principal axes. The same situation happens for Poisson's ratio in cubic symmetry. Negative Poisson's ratios have been observed in some minerals at certain directions. Several authors have reported negative Poisson's ratios in some anisotropic crystals (Alderson and Evans, 2002; Baughman et al., 2000 and etc.).

4.3 Dynamic and static mechanism

Although dynamic and static moduli are measured under different mechanism, strong correlations have been reported for rocks like granite, limestone, and sandstone (Mavko, et al., 1998). Static moduli are usually involved in the estimation of brittleness. On the other hand, the static method is time consuming and destructive to samples. The correlation between static and dynamic is important for reservoir analysis if such a relation could be found for certain type of rocks, then the static modulus in situ conditions can be estimated from elastic waves. Mechanical properties on shale plugs with different orientations were measured to evaluate anisotropic properties of strength and deformation, including dynamic elastic anisotropy (via wave propagation at a central frequency of 1 MHz).

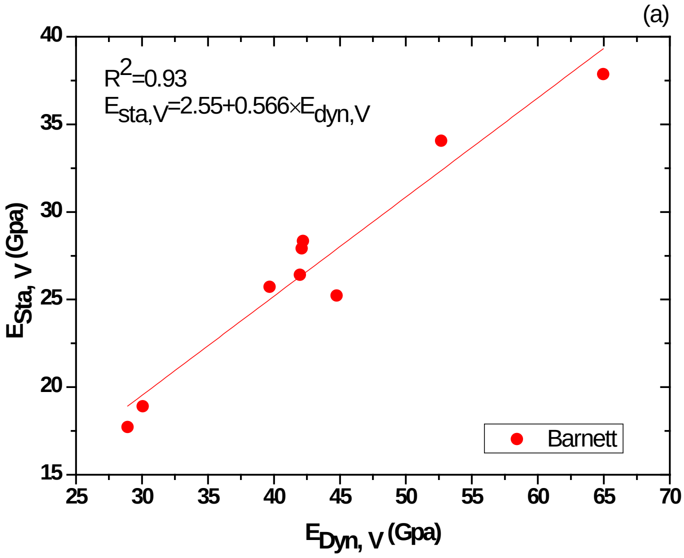

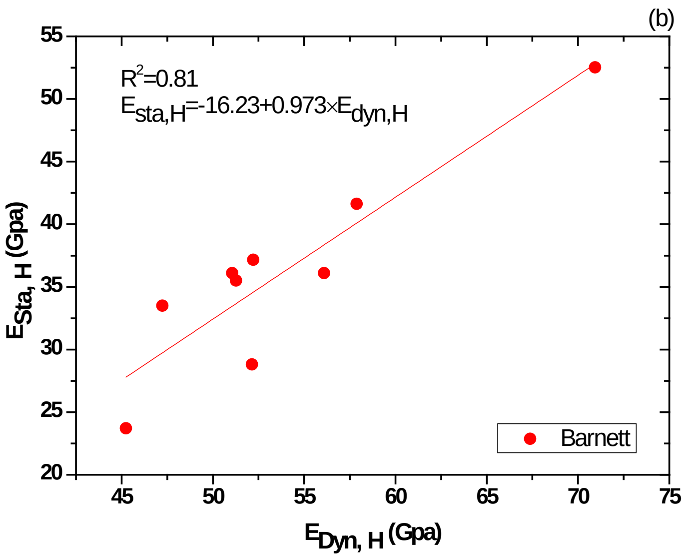

Figure 4-1: (a) Static vs. dynamic relation for vertical Young's modulus derived from Marathon Barnett shale dataset. (b) Static vs. dynamic relation for horizontal Young's modulus derived from Marathon Barnett shale dataset.

We plot correlation of static and dynamic Young's modulus in the vertical and horizontal directions to the symmetry axes for Barnett shale are seen in Figure 4-1. Empirical relations between the dynamic and static Young's modulus in both vertical and horizontal directions have been derived as,

$$E_{sta,V} = 2.55 + 0.566 \times E_{Dyn,V} \tag{4-3}$$

$$E_{sta,H} = -16.23 + 0.973 \times E_{Dyn,H} \tag{4-4}$$

Since our shale data is limited, more statistical measurements should be made to verify the empirical relationships for Barnett shale.

4.4 Effects of porosity and mineral composition on the rock mechanical properties

Porosity reflects the degree of void space in a porous rock. The mechanical response of rock formation to stress and pore pressure was reported as the theory of poroelasticity (Biot 1941). Since Barnett shale is siliceous shale abundant in clay and quartz, an effort was made to study how the Young's modulus was affected by porosity, clay and TOC, carbonate, and quartz, respectively.

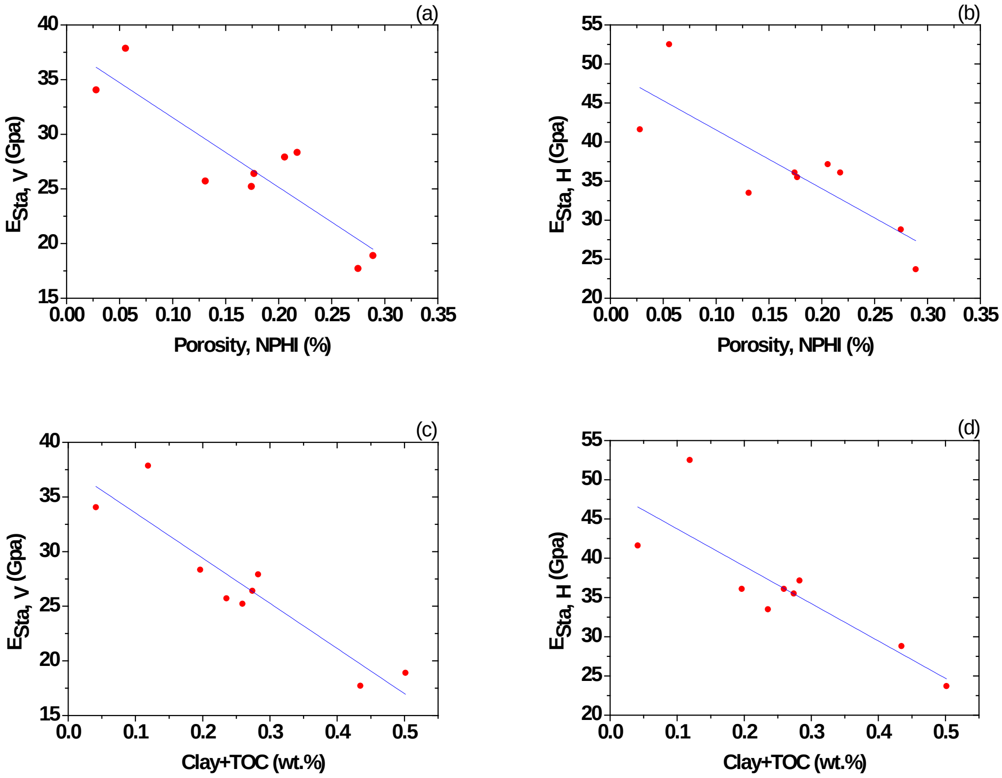

Figure 4-2: Effects of porosity and clay plus TOC on the Young's modulus, (a) Vertical Young's modulus (static) vs. neutron porosity. (b) Horizontal Young's modulus (static) vs. neutron porosity. (c) Vertical Young's modulus (static) vs. clay and TOC contents. (d) Horizontal Young's modulus (static) vs. clay and TOC contents. Data come from Marathon Barnett shale dataset.

Figure 4-2 shows the effects of porosity and clay mineral plus TOC on the vertical and horizontal Young's modulus. Pore spaces and the 'soft' clay and organic matters have the same effect on the compressibility of rock formation, which reduces the rock rigidity in similar trend.

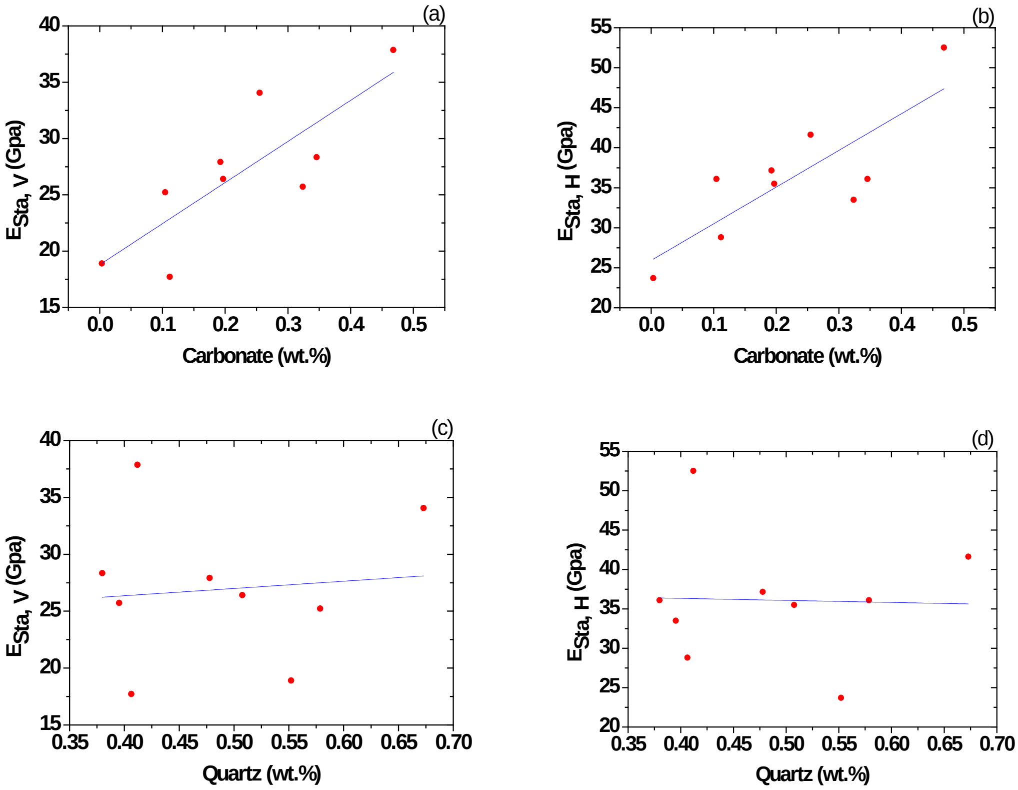

Figure 4-3: Effects of carbonate and quartz on the Young's modulus, (a) Vertical Young's modulus (static) vs. carbonate. (b) Horizontal Young's modulus (static) vs. carbonate. (c) Vertical Young's modulus (static) vs. quartz. (d) Horizontal Young's modulus (static) vs. quartz. Data come from Marathon Barnett shale dataset.

Figure 4-3 shows the effects of carbonate minerals and quartz on the vertical and horizontal Young's modulus. In general, these 'hard' minerals as carbonate and quartz have the same effect on the compressibility of rock formation, which increases the rock rigidity.

4.5 Relationship between Young's modulus, Poisson's ratio and Thomsen anisotropy parameters

The elasticity parameters are essential to estimate the Young's modulus and Poisson's ratio. However, most estimations are based on the isotropic assumption. In presence of bedding planes, strong anisotropy of shale formation needs to be considered. Chesnokov et al. (2010) discussed a technique allowing inversion of the shale stiffness tensor with VTI symmetry from standard logging data.

The anisotropic Young's modulus and Poisson's ratio also can be derived from the five independent elastic constants for VTI medium (Appendix A). The elastic constants can be normalized with respect to C_{33} (Banik et al., 2012), which are written as,

$$C'_{33} = \frac{C_{33}}{C_{33}} = 1 \tag{4-5}$$

$$C'_{44} = \frac{C_{44}}{C_{33}} = \xi^2 \tag{4-6}$$

$$C'_{66} = \frac{C_{66}}{C_{33}} = (1 + 2\gamma)\xi^2 \tag{4-7}$$

$$C'_{11} = \frac{C_{11}}{C_{33}} = 1 + 2\varepsilon \tag{4-8}$$

$$C'_{13} = \frac{C_{13}}{C_{33}} = \sqrt{(1 - \xi^2)^2 + 2\delta(1 - \xi^2)} - \xi^2 \tag{4-9}$$

$$C'_{12} = \frac{C_{12}}{C_{33}} = 1 + 2\varepsilon - 2\xi^2(1 + 2\gamma) \tag{4-10}$$

Where the parameter ξ is the square of velocity ratio Vs/Vp, $\xi^2 = C_{55}/C_{33} = (Vs/Vp)^2$.

Equations (4-5) – (4-10) can be substituted in the expressions A-16 and A-17 provided in appendix A, then the Young's modulus and Poisson's ratio can be expressed in terms of the Thomsen anisotropy parameters and the velocity ratio parameter ξ, where $E_H = E_{11}$, $E_V = E_{33}$, $\nu_H = \nu_{12}$, and $\nu_V = \nu_{13}$. The subscript "H" and "V" represents "Horizontal" and "Vertical", respectively.

$$E_H^{'} = 4\xi^2(1+2\gamma)\left(1 - \frac{\xi^2(1+2\gamma)}{1+2\varepsilon-(\sqrt{(1-\xi^2)^2+2\delta(1-\xi^2)}-\xi^2)^2}\right) \tag{4-11}$$

$$E_V^{'} = 1 - \frac{(\sqrt{(1-\xi^2)^2+2\delta(1-\xi^2)}-\xi^2)^2}{1+2\varepsilon-\xi^2(1+2\gamma)} \tag{4-12}$$

$$\nu_H = 1 - \frac{2\xi^2(1+2\gamma)}{1+2\varepsilon-(\sqrt{(1-\xi^2)^2+2\delta(1-\xi^2)}-\xi^2)^2} \tag{4-13}$$

$$\nu_V = \frac{\sqrt{(1-\xi^2)^2+2\delta(1-\xi^2)}-\xi^2}{2+4\varepsilon-2\xi^2(1+2\gamma)} \tag{4-14}$$

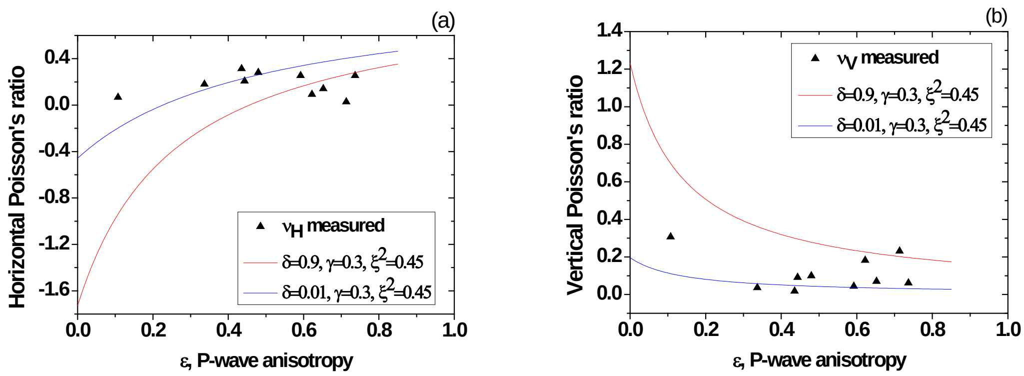

Figure 4-4. (a) Horizontal Poisson's ratio as a function of ε and two different values of δ compared with that calculated from velocity measurements. (b) Vertical Poisson's ratio as a function of ε and two different values of δ compared with that calculated from velocity measurements.

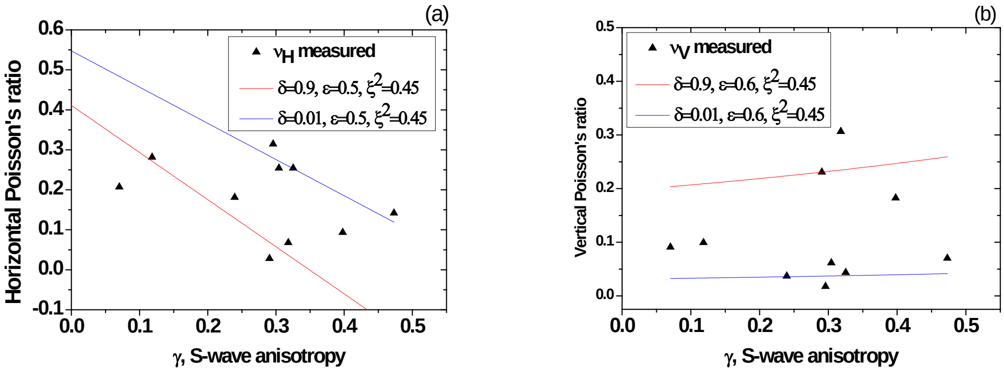

Figure 4-5. (a) Horizontal Poisson's ratio as a function of γ and two different values of δ compared with that calculated from velocity measurements. (b) Vertical Poisson's ratio as a function of γ and two different values of δ compared with that calculated from velocity measurements.

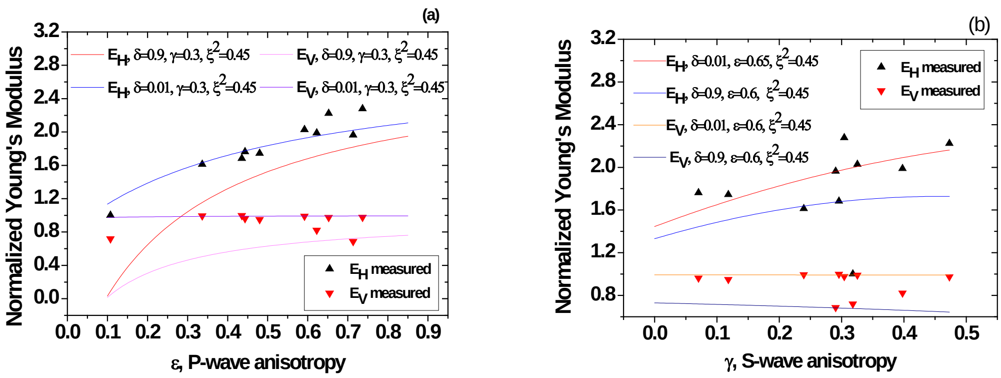

Figure 4-6. (a) Normalized vertical and horizontal Young's modulus as a function of ε and two different values of δ compared with that calculated from velocity measurements. (b) Normalized vertical and horizontal Young's modulus as a function of γ and two different values of δ compared with that calculated from velocity measurements.

The Young's modulus and Poisson's ratio changing with Thomson anisotropy parameters ε, γ, and δ were plotted in Figure 4-4 to Figure 4-6. The laboratory measurements were added to compare with the theoretical curves. The vertical Poisson's ratio and horizontal Poisson's ratio change in opposite direction, the horizontal Poisson's ratio increases with ε while the vertical Poisson's ratio decreases. For parameter γ, the horizontal Poisson's ratio decreases while the vertical Poisson's ratio increases slightly with increase in γ. On the other hand, the horizontal Young's modulus increases with both ε and γ, while the vertical Young's modulus increase slightly with ε and decreases slightly with γ. The measurements results are mostly located in the range of curves with different relevant parameters, which fit the theoretical trend quite well.

4.6 Summary

Cubic minerals show a behavior similar to isotropy, mainly because cubic symmetry attains the same value along principal axes. Compared with the isotropic case, negative Poisson's ratios have been observed in some minerals along certain directions.

Obtained results show, that the dynamic Young's modulus is greater than the static one, the static/dynamic Young's modulus ratio ranges from 0.52 to 0.74. The ratio of static/dynamic is different in the vertical and horizontal directions, which reflects the anisotropy properties of Barnett shales. Empirical relations between static and dynamic Young's modulus have been proposed for Barnett shale. The confining pressure was not considered in correlating the dynamic and static properties, as we assume that it has the same effect on static and dynamic deformation processes.

The pores and cracks in shales, are the intrinsic causes of static/dynamic modulus difference. The mineral compositions contribute their unique effects on the compressibility of shales. The anisotropy on Young's modulus and Poisson's ratio behave differently in respect to the Thomson anisotropy parameters.

Chapter 5 Determining Shale Properties with Mathematical Modeling

5.1 Introduction

Rocks like shale have complex mineral compositions and microstructures, which exhibit high heterogeneity. In order to estimate the general (effective) physical properties of a heterogeneous medium, the effective medium theory was introduced by assuming the wavelength is much greater than the size of heterogeneity (Eshelby, 1957; Hudson, 1981; Hornby et al., 1994; Bayuk et al. 2007). This theory was applied to predict the effective elastic or transport properties from the inner structure (isotropic or anisotropic matrix) and concentration of inclusions (pores, shapes, and connection). Statistical averaging procedures were used on inhomogeneous anisotropic multicomponent media. Different effective medium theories have their own limitations based on different assumptions, focusing on either inclusions or the matrix. Shermergor (1977) developed the General Singular Approximation (GSA) method, which can estimate the effective properties with the best match to various laboratory data (Bayuk and Chesnokov, 1998).

5.2 General singular approximation method

Shermergor (1977) described the basic relationship between stress, strain, and stiffness tensors, in random inhomogeneous arbitrary anisotropic medium as the following forms:

$$\begin{aligned} \sigma_{ij}(x) &= \langle \sigma_{ij} \rangle + \sigma'_{ij}(x), \\ \varepsilon_{ij}(x) &= \langle \varepsilon_{ij} \rangle + \varepsilon'_{ij}(x) \\ C_{ijkl}(x) &= \langle C_{ijkl} \rangle + C'_{ijkl}(x) \end{aligned} \quad (5\text{-}1)$$

where $\sigma_{ij}(x)$, $\varepsilon_{ij}(x)$, and $C_{ijkl}(x)$ are stress, strain, and the stiffness tensor at a point x; And $\sigma'_{ij}(x)$, $\varepsilon'_{ij}(x)$, and $C'_{ijkl}(x)$ represent the fluctuations of stress, strain and the stiffness tensor at a point x. The brackets $< >$ represent the averaged value over a volume where the medium is statistically homogeneous,

$$\langle \sigma \rangle \equiv \frac{1}{V} \int_V \sigma(r) dr, \text{ and } \langle \varepsilon \rangle \equiv \frac{1}{V} \int_V \varepsilon(r) dr \quad (5\text{-}2)$$

Hook's law is given by:

$$\sigma_{ij}(x) = C_{ijkl}(x) \varepsilon_{kl}(x) \quad (5\text{-}3)$$

Substituting equation (5-2) with (5-1) and averaging it, we can get the form,

$$\langle \sigma_{ij} \rangle = C^*_{ijkl} \langle \varepsilon_{kl} \rangle \quad (5\text{-}4)$$

where $C^*_{ijkl}(x)$ is an effective stiffness tensor.

The general singular approximation method (Shermergor, 1997 and Willis, 1977) can be used to calculate the effective stiffness tensor. The derivation is based on the comparison of the displacement fields between a heterogeneous original body and a homogeneous reference body at the same boundary condition,

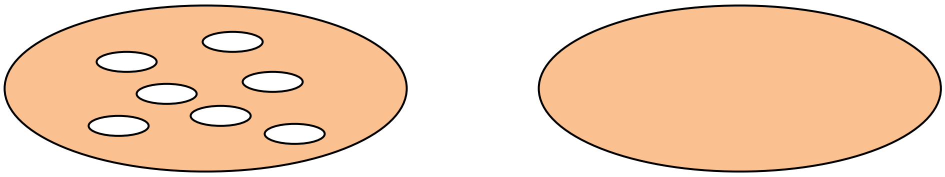

Heterogeneous body with unknown C* Homogeneous body with Known C^c

Figure 5-1. The inhomogeneous original body and the homogeneous comparison body. (Pictures revised after Tao, PhD Dissertation, 2013)

The unknown effective elastic constant C* of the studied inhomogeneous original body shown in figure 5-1 is a 4th rank tensor. While C^c is the elastic constant of the "comparison homogeneous body". It's assumed that the strain and stress fields are related in Hook's law for both bodies. The following equilibrium equation is assumed to be true for the original and comparison body, respectively,

$$Lu = -f \tag{5-5}$$

$$L^c u^c = -f \tag{5-6}$$

Where vector f is the density of volume force and U is the displacement vector. The operator L has the form (U^c and L^c are notation for the comparison body),

$$L_{ik} = \nabla_j C_{ijkl} \nabla_l \tag{5-7}$$

C_{ijkl} is the 4^{th} rank stiffness tensor in the inhomogeneous original body.

Because the comparison body and original body share the same boundary condition, then subtracting equation (5-6) from (5-5):

$$L^c u' = L' u \tag{5-8}$$

Where $U' = U - U^c$ and $L' = L - L^c$. This can be solved by introducing the Green's tensor G of operator L^c with below formula,

$$L^c G = -I\delta(r) \tag{5-9}$$

Where I is the 4th rank unit tensor defined by $I_{ijkl} = \frac{1}{2}(\delta_{il}\delta_{jk} + \delta_{ik}\delta_{jl})$ and δ is the Kronecker delta,

$$\delta_{ij} = \begin{cases} 0 \ if \ i \neq j \\ 1 \ if \ i = j \end{cases} \tag{5-10}$$

From equation (5-9) we can get,

$$U' = G * L'U \tag{5-11}$$

the sign '$*$' means the convolution with Green's function. For the elastic case,

$$u'_j(r) = \int_V G_{ij}(r - r')L'_{ik}(r')u_k(r')dr' \tag{5-12}$$

where $G_{ij}(r - r')$ is the displacement solution at location r caused by the source at location r' and i,j are coordinate. The stiffness tensor will be constant to the coordinates if the medium is statistical homogeneous. Then from equation (5-7) we can get,

$$L'_{ik}u_k = C'_{ijkl}u_{k,lj} = C'_{ijkl}\varepsilon_{kl,j} \tag{5-13}$$

Substituting equation (5-13) into equation (5-12), we have

$$u'_m(r) = \int_V G_{im}(r - r')C'_{ijkl}\varepsilon_{kl,j}(r')dr' \tag{5-14}$$

Replacing index m with n gives,

$$u'_n(r) = \int_V G_{in}(r - r')C'_{ijkl}\varepsilon_{kl,j}(r')dr' \tag{5-15}$$

Applying the operator $\frac{\partial}{\partial x_n}$ to equation (5-14) and $\frac{\partial}{\partial x_m}$ to equation (5-15), and adding the results,

$$u'_{m,n}(r) + u'_{n,m}(r) = \int_V [G_{im,n}(r - r') + G_{in,m}(r - r')]C'_{ijkl}\varepsilon_{kl,j}(r')dr' \quad (5\text{-}16)$$

Appling integration by parts with the boundary terms equal to zero, gives

$$\varepsilon'_{mn}(r) = \int_V g_{imjn}(r - r')C'_{ijkl}\varepsilon_{kl}(r')dr' \quad (5\text{-}17)$$

Where $g_{imjn} = \frac{1}{2}(G_{im,jn} + G_{jm,in})$, $\varepsilon'_{mn} = \varepsilon_{mn} - \varepsilon^c_{mn}$, and $C'_{ijkl} = C_{ijkl} - C^c_{ijkl}$. And $G_{ij,mn}$ is the 2nd order derivative of the Green's function with respect to m and n coordinates. Equation (5-17) can be further simplified by using an integral operator Q,

$$\varepsilon'_{mn}(r) = Q_{imjn}C'_{ijkl}\varepsilon_{kl}(r') \quad (5\text{-}18)$$

Meanwhile, the fluctuation of strain difference can be represented as,

$$\varepsilon'' = \varepsilon' - \langle\varepsilon'\rangle \quad (5\text{-}19)$$

Where $\varepsilon' = \varepsilon - \varepsilon^c$, which is the strain difference between the original and comparison body and $\langle\varepsilon\rangle$ represents the volume average. If we substitute equation (5-18) into (5-19),

$$\varepsilon'' = QC'\varepsilon - Q\langle C'\varepsilon\rangle \quad (5\text{-}20)$$

Considering the definition of effective stiffness from equations (5-3) and (5-4) gives,

$$\langle C\varepsilon\rangle = \langle\sigma\rangle = C^*\langle\varepsilon\rangle \quad (5\text{-}21)$$

As C^c is constant, we have,

$$\langle C'\varepsilon\rangle = \langle(C - C^c)\varepsilon\rangle = \langle C\varepsilon\rangle - \langle C^c\varepsilon\rangle = C^*\langle\varepsilon\rangle - C^c\langle\varepsilon\rangle = C'^*\langle\varepsilon\rangle \quad (5\text{-}22)$$

Where $C'^{*} = C^{*} - C^{c}$, thus we substitute (5-22) into (5-20),

$$\varepsilon'' = QC'\varepsilon - QC'^{*}\langle\varepsilon\rangle \tag{5-23}$$

Also we substitute $\varepsilon' = \varepsilon - \varepsilon^{c}$ to (5-19),

$$\varepsilon'' = \varepsilon - \varepsilon^{c} - \langle\varepsilon - \varepsilon^{c}\rangle = \varepsilon - \langle\varepsilon\rangle \tag{5-24}$$

Substituting (5-24) into (5-23) gives,

$$\varepsilon - \langle\varepsilon\rangle = QC'\varepsilon - QC'^{*}\langle\varepsilon\rangle \tag{5-25}$$

Then we can have,

$$\varepsilon = (I - QC')^{-1}(I - QC'^{*})\langle\varepsilon\rangle \tag{5-26}$$

Thus

$$I - QC'^{*} = \left\langle (I - QC')^{-1} \right\rangle^{-1} \tag{5-27}$$

Substituting (5-27) into (5-25) gives

$$\varepsilon = (I - QC')^{-1}\left\langle (I - QC')^{-1} \right\rangle^{-1}\langle\varepsilon\rangle \tag{5-28}$$

Substituting the above equation back into the effective stiffness (5-23), the final algorithm to calculate the effective stiffness in the elastic case can be derived as,

$$C^{*} = \left\langle C(I - QC')^{-1} \right\rangle \left\langle (I - QC')^{-1} \right\rangle^{-1} \tag{5-29}$$

where C* is the effective stiffness of the target body. Angle brackets are symbols of the volume average and C is the stiffness tensor. Q is an integral operator over coordinates, which means the convolution of the derivatives of the Green's function. C' is the stiffness difference between the target and comparison body, $C' = C - C^{c}$.

5.3 Elastic properties for common minerals in the Barnett shale

Shale can be classified by its mineral content. Usually they can be recognized as carbonate-rich or siliceous shales. Barnett shale is a siliceous shale, with dark brown or black color. They have a relatively large content of siliceous minerals (such as quartz, feldspar, and clay) but with fewer carbonate minerals (such as calcite and dolomite).

The single minerals in Barnett shale are different in its stiffness tensors symmetry system density and elastic modulus. In this study, we use the elastic properties of single minerals in the Barnett shale to estimate the elastic properties of the whole rock by assuming their elastic constants are stable. Table 5-1 presents the elastic constants and density of the most common minerals in the Barnett Shale.

Table 5-1: The stiffness tensors of common minerals in Barnett shale.

C_{ij}	**Qua**	**Cal**	**Dol**	**Alb**	**Pyr**	**Ort**	**Ill**	**Kao**	**Chl**	**Sid**	**Apa**	**Ara**	**Hal**
C11	86	144	205	74	361	67	179.9	172	182	229	140	160	49.1
C12	7.4	53.9	71	36.3	33.6	45.3				112	13	37.3	14
C13	11.91	51.1	57.4	37.6		26.5	14.5	27.1	20.3	75	69	1.7	
C14	-18.04	-20.5	-19.5							14			
C15			13.7	-9.1		-0.2							
C22	86	144	205	137.5		169				229		87.2	
C23	11.91	51.1	57.4	32.6		20.4				75		15.7	
C24	18.04	20.5	19.5							-14			
C25			-13.7	-10.4		-12.3							
C26													
C33	105.8	84	113	128.9		118	55	52.6	107	125	180	84.8	
C34													
C35				-19.1		-15							
C44	58.2	33.5	39.8	17.2	105	14.3	11.7	14.8	11.4	41	36.2	41.3	12.7
C45													
C46			-13.7	-1.3		-1.9							
C55	58.2	33.5	39.8	30.3		23.8				41		25.6	
C56	-18.04	-20.5	-19.5							14			
C66	39.3	45.05	67	31.1		36.4	70	66.3	62.5	58.5	63.5	42.7	
ρ	2.65	2.712	2.87	2.62	5.02	2.56	2.79	2.52	2.68	3.96	3.146	2.93	2.16

Note: The abbreviations of minerals are, 'Qua-Quartz, Cal-Calcite, Dol-Dolomite, Alb-Albite, Pyr-Pyrite, Ort-Orthoclase, Ill-Illite, Kao-Kaolinite, Chl-Chlorite, Sid-Siderite, Apa-Apatite, Ara-Aragonite, and Hal-Halite'. Where ρ *is density with unit g/cm*^{3}.

Table 5-2 presents the symmetry systems of single minerals. The number of independent elastic constants is unique to each type of symmetry system. We have derived the anisotropic formulae for several symmetry systems in Appendix A.

Table 5-2: The symmetry system of common minerals in Barnett shale.

Mineral	**Symmetry**	**References**
Pyrite	Cubic	Bass (1995)
Halite	Cubic	Bass (1995)
Illite	Hexagonal	Alexandrov and Ryzhova, (1961)
Kaolinite	Hexagonal	Alexandrov and Ryzhova, (1961)
Apatite	Hexagonal	Bass (1995)
Chlorite	Hexagonal	Alexandrov and Ryzhova, (1961)
Albite	Monoclinic	Belikov et al. (1970)
Orthoclase	Monoclinic	Bass (1995)
Aragonite	Orthorhombic	Bass (1995)
Calcite	Trigonal	Peselnick and Robie (1963)
Dolomite	Trigonal	Bass (1995)
Siderite	Trigonal	Bass (1995)
Quartz	Trigonal	Belikov et al. (1970)

5.4 Workflow and data required for GSA modeling

In GSA modeling, shale can be simulated as a medium with matrix plus inclusions. Clay minerals are usually assumed as the solid matrix for shale. The inclusion are composed of 'solid' inclusions, such as quartz, feldspar, calcite, and other common minerals in shale, or 'fluid' inclusions as pores filled with gas, oil, and brine water, or a combination of all. Hornby et al. (1994) pointed out that the matrix should be modeled first, then the inclusions can be added in as a second stage modeling. Therefore the workflow would be divided into two stages,

1) Stage 1, modeling solid shale with solid inclusions embedded in clay matrix: approximated by the effective stiffness tensor for the solid shale by using the density, elastic constants, and volume concentration of clay minerals and all

other minerals (quartz, feldspar, pyrite, and dolomite, etc.). In this stage, 'fluid' inclusions are not included.

2) Stage 2, modeling the whole shale with fluid inclusions in solid matrix: approximated by the effective stiffness tensor for the whole rock, by introducing pores into the solid shale, with the proper saturation of gas, oil, and the medium are used to control the pore shapes and connectivity.

Friability (f) is an empirical parameter that reflects the connectivity of pores. The value of friability ranges from 0 to 1. The friability is 0 when inclusions are isolated and the friability is 1 when inclusions are all connected. Aspect ratio defines the geometric shape of the inclusions, which is the ratio of short axes to long axes with a range of [0,1]. The restriction for the friability and aspect ratio of pores and other inclusions are based on the analysis of SEM images.

The mineralogy composition required for the modeling comes from XRD results. XRD results for twelve Barnett shale cores from Devon Energy Co. are listed in Table 3-1 and the XRD results for cores from Marathon dataset were provided by Terra Tech. The elastic constants of single mineral are listed in Table 5-1. Density and porosity for cores are also required in the modeling processes.

Table 5-3: The parameters used in the modeling.

Porosity Ø	1% - 11% from core measurement
Friability *f*	0.1 – 0.3 (adjusted on inversion results)
Aspect ratio	0.1 – 0.5 (based on the assumption of pore geometry)
Inclusion	Gas, 0.0001Gpa bulk modulus, 0.0013 density

We summarized the input parameter for modeling in Table 5-3. The porosity was measured in the laboratory with dry samples. Friability range was based the on the best fitting inversion results. If the aspect ratio was less than 0.5 as we assume the majority of pores are thin, ellipsoidal shape oriented along the bedding plane. Gas was chosen as the pore fluid for Barnet shale, as it is a kind of highly matured gas shale.

5.5 Results of GSA modeling method

The effective stiffness tensors of the shale modeled from the GSA method are used to calculate the vertical P- and S-wave velocities and are then compared with the ultrasonic velocities measured in the laboratory and the velocities acquired from sonic well-log tools.

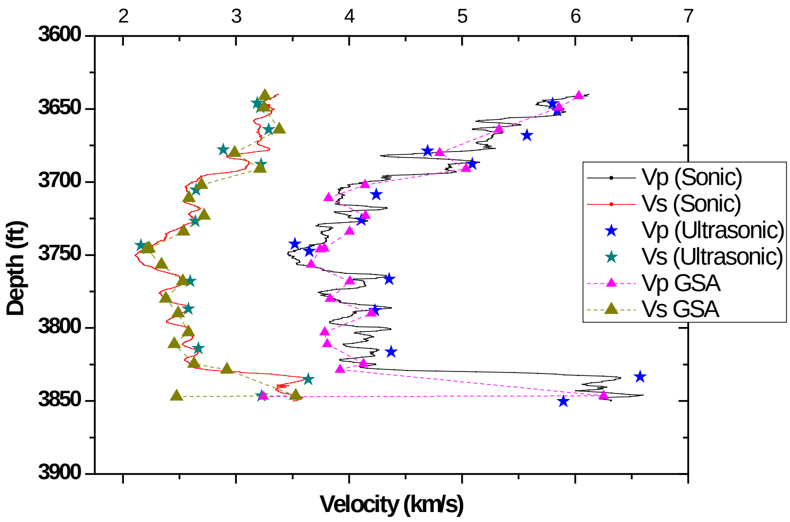

Figure 5-2. The comparison of vertical Vp and Vs derived from GSA modeling (triangle symbol with dash lines) with that measured in laboratory at ultrasonic frequency (star symbols) and that measured from well-log tools at sonic frequency (solid lines).

Figure 5-2 shows the modeling results can fit the measured results successfully. With optimized parameters based on the microstructure properties of shale, effective elastic constants can be simulated successfully. The difference between laboratory measurements and well-log tools mainly reflect the wave velocity scattering at different frequencies.

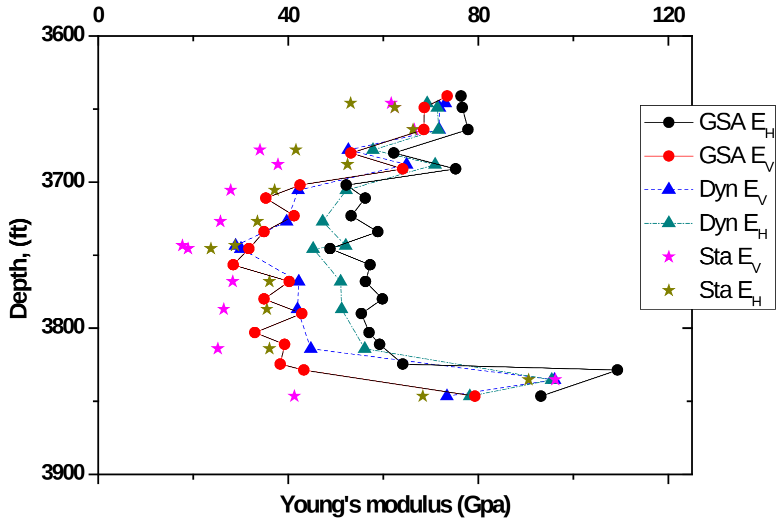

Figure 5-3. The anisotropic Young's modulus derived from effective elastic constants from GSA method compared with dynamic and static Young's modulus.

Anisotropic Young's modulus measured and estimated from three different methods are compared in Figure 5-3. The dynamic Young's modulus is always higher than the static one, which reflects the various degree of deformation for static and dynamic measurements. As the modeled Young's modulus are derived from the effective elastic constants, then it obviously will be matched with the dynamic modulus.

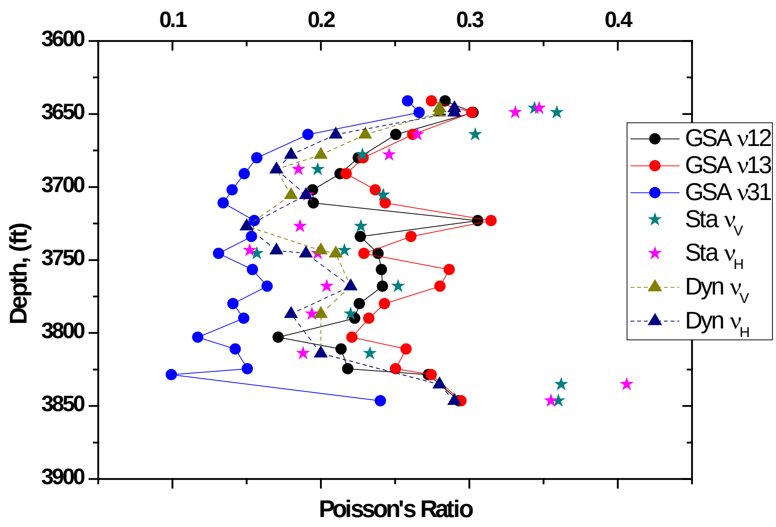

Figure 5-4. The anisotropic Poisson's ratio (three directions) derived from effective elastic constants from GSA method compared with dynamic and static Poisson's ratio (two directions).

Anisotropic Poisson's ratio calculated from measurements and estimated from GSA methods are compared in Figure 5-4. Taking anisotropy into consideration, the data from dynamic or static measurements lies between the three components of Poisson's ratio estimated from modeling. The two vertical and one horizontal Poisson's ratio provided by GSA modeling give the chance to understand the mechanical properties of shale layers in a three dimensional view.

5.6 Summary

The anisotropic Young's modulus and Poisson's ratio estimated from modeling effective elastic constants show good a fit with the measured modulus. This means the GSA method is useful to estimate the elastic anisotropy and mechanical properties of shale plays. Understanding of the microstructure can help setting strict constraints on the input parameters, with which the effective elastic constants can be modeled. With the comparison of core laboratory measurements or sonic log data, the effectiveness of modeling can be controlled. With derived effective elastic constants, the anisotropic behavior of mechanical properties can be studied in all dimensions. GSA methods offer a feasible way to interpret a reservoir` of shale plays.

Chapter 6　Conclusion and Discussion

We investigated the elastic properties, permeability, and mechanical properties of Barnett shale samples from Fort Worth Basin. A new method was proposed to improve the accuracy of velocity and permeability measurements. Based on the microstructure and other elastic properties we studied, a mathematical model using the GSA method was applied to simulate the gas shale medium. The results of our measurements and data analysis show that,

1. For shale elasticity measured in the laboratory, the accuracy is quite dependent on the velocity measured at 45 degrees. In order to derive the accurate elastic constant C13, we introduced a new method to consider both Vp and Vsv to calibrate the cutting angle. By calibrating the cutting angle error, the accuracy has been improved for both velocity measurements and permeability tensor measurements. Furthermore, this new technique can be applied to not only the three-plug method but also the single-plug ultrasonic measurement.

2. Barnett shale shows high anisotropic properties. The p-wave anisotropy parameter ε reaches up to 73% and the S-wave parameter γ reaches up to 47% at unconfined conditions. Thomsen P- and S-wave anisotropy parameters were found to increase, with the increase of clay and organic content, and decrease with the increase of carbonate contents. Unconfined shale samples display higher anisotropy and more scattering in Thomsen anisotropy parameters, which may be caused by the cracks and fractures developed under room condition. The Vp/Vs

ratio of Barnett shale ranges from 1.5 to 1.8, which is consistent with other shale data in literatures. We also found the correlation between vertical and horizontal velocity for shales. This empirical relation will be extremely useful to study the anisotropic properties of shale reservoirs when only vertical well-logs are available.

3. Permeability is much more sensitive than velocity to the existing anisotropy. The permeability parallel to bedding plane is usually two orders larger in magnitude than that normal to bedding. Along the symmetry axes, permeability anisotropy has a good correlation with velocity anisotropy, even though they have different physical mechanisms. The highest permeability and highest velocity can be expected along the bedding planes of shales. Empirical relations have been developed between permeability and elastic constant C44, which may be used to estimate permeability from wave propagation for VTI rocks.
4. From the single mineral study in this dissertation, the Young's modulus and Poisson's ratio vary dramatically between average isotropic and anisotropic cases. Negative Poisson's ratio has been observed in some directions for certain minerals. Cubic symmetry minerals have the same Young's modulus or Poisson's ratio along principle axes. Dynamic Young's modulus is greater than the static one, the static/dynamic Young's modulus ratio ranges from 0.52 to 0.74. Empirical relations between static and dynamic Young's modulus have been suggested in both the vertical and horizontal directions. The porosity, clay, and TOC tend to decrease the compressibility of the solid rocks. While the 'hard' minerals like quartz, feldspar, and carbonate tend to increase the compressibility. The anisotropic Young's

modulus and Poisson’s ratio behave differently in respect to the Thomson anisotropy parameters.

5. The effective medium model conducted in this dissertation is the GSA method, which has been proven to be useful to estimate the elasticity of shale. Mathematical models can be constructed successfully by understanding microstructure properties like pore shape, distribution, connectivity, and mineral compositions. The elastic constants derived from the GSA model fit well with the results from laboratory measurements and well-log data. Therefore, the anisotropic behavior of mechanical properties can be interpreted for shale reservoirs.

We want to point out that more statistical studies need to be conducted in order to verify the empirical relations observed. Simultaneously measuring elasticity and permeability at the same conditions is suggested, to study the inter-correlation between wave propagation and fluid flow. In this dissertation, the GSA method was applied successfully to discrete core samples. The extension of this effective medium theory for formation analysis by using standard well-log data can also be one for future research.

Appendix A: The Poisson's ratio and Young's modulous for medium with different type of symmetry

In general, the stress and stain relationship for linear elastic material without initial stress can be described by Hooke's law as (Timoshenko and Goodier, 1934),

$$\sigma_{ij} = C_{ijkl}\varepsilon_{kl} \tag{A-1}$$

Where σ_{ij} and ε_{kl} are the elements of the stress and strain tensors, C_{ijkl} are the elastic stiffness constants. Also it can be written as the relationship between stress and strain,

$$\varepsilon_{ij} = S_{ijkl}\sigma_{kl} \tag{A-2}$$

Where S_{ijkl} are elastic compliance constants.

For an orthorhombic type of symmetry, the matrix of elastic constants has a form,

$$C_{mn} = \begin{pmatrix} C_{11} & C_{12} & C_{13} & 0 & 0 & 0 \\ C_{12} & C_{22} & C_{23} & 0 & 0 & 0 \\ C_{13} & C_{33} & C_{33} & 0 & 0 & 0 \\ 0 & 0 & 0 & C_{44} & 0 & 0 \\ 0 & 0 & 0 & 0 & C_{55} & 0 \\ 0 & 0 & 0 & 0 & 0 & C_{66} \end{pmatrix} \qquad S_{mn} = \begin{pmatrix} S_{11} & S_{12} & S_{13} & 0 & 0 & 0 \\ S_{12} & S_{22} & S_{23} & 0 & 0 & 0 \\ S_{13} & S_{33} & S_{33} & 0 & 0 & 0 \\ 0 & 0 & 0 & S_{44} & 0 & 0 \\ 0 & 0 & 0 & 0 & S_{55} & 0 \\ 0 & 0 & 0 & 0 & 0 & S_{66} \end{pmatrix} \tag{A-3}$$

So equation A-1 can be expressed in a component form as,

$$\sigma_{11} = C_{11kl}\varepsilon_{kl} = C_{11}\varepsilon_{11} + C_{12}\varepsilon_{22} + C_{13}\varepsilon_{33}$$

$$\sigma_{22} = C_{22kl}\varepsilon_{kl} = C_{12}\varepsilon_{11} + C_{22}\varepsilon_{22} + C_{23}\varepsilon_{33}$$

$$\sigma_{33} = C_{33kl}\varepsilon_{kl} = C_{13}\varepsilon_{11} + C_{23}\varepsilon_{22} + C_{33}\varepsilon_{33}$$

$$\sigma_{12} = C_{12kl}\varepsilon_{kl} = 2C_{66}\varepsilon_{12}$$

$$\sigma_{13} = C_{13kl}\varepsilon_{kl} = 2C_{55}\varepsilon_{13}$$

$$\sigma_{23} = C_{23kl}\varepsilon_{kl} = 2C_{44}\varepsilon_{23}$$

(A-4)

Equation A-2 also can be expressed in a component form as,

$$\varepsilon_{11} = S_{11kl}\sigma_{kl} = S_{11}\sigma_{11} + S_{12}\sigma_{22} + S_{13}\sigma_{33}$$

$$\varepsilon_{22} = S_{22kl}\sigma_{kl} = S_{12}\sigma_{11} + S_{22}\sigma_{22} + S_{23}\sigma_{33}$$

$$\varepsilon_{33} = S_{33kl}\sigma_{kl} = S_{13}\sigma_{11} + S_{23}\sigma_{22} + S_{33}\sigma_{33}$$

$$\varepsilon_{12} = S_{12kl}\sigma_{kl} = 2S_{66}\sigma_{12}$$

$$\varepsilon_{13} = S_{13kl}\sigma_{kl} = 2S_{55}\sigma_{13}$$

$$\varepsilon_{23} = S_{23kl}\sigma_{kl} = 2S_{44}\sigma_{23}$$

(A-5)

In order to find S_{ijkl} as a function of C_{ijkl}, we have to solve algebraic system of equation A-4 with the respect to εij and compare the obtained results with original system in equation A-5. From equations of A-4, we can get,

$$\varepsilon_{11} = \frac{\begin{pmatrix} \sigma_{11} & C_{12} & C_{13} \\ \sigma_{22} & C_{22} & C_{23} \\ \sigma_{33} & C_{23} & C_{33} \end{pmatrix}}{\begin{pmatrix} C_{11} & C_{12} & C_{13} \\ C_{12} & C_{22} & C_{23} \\ C_{13} & C_{23} & C_{33} \end{pmatrix}} = \frac{(C_{22}C_{33} - C_{23}^2)}{D}\sigma_{11} + \frac{(C_{13}C_{23} - C_{12}C_{33})}{D}\sigma_{22} + \frac{(C_{12}C_{23} - C_{13}C_{22})}{D}\sigma_{33}$$

$$\varepsilon_{22} = \frac{\begin{pmatrix} C_{11} & \sigma_{11} & C_{13} \\ C_{12} & \sigma_{22} & C_{23} \\ C_{13} & \sigma_{33} & C_{33} \end{pmatrix}}{\begin{pmatrix} C_{11} & C_{12} & C_{13} \\ C_{12} & C_{22} & C_{23} \\ C_{13} & C_{23} & C_{33} \end{pmatrix}} = \frac{(C_{13}C_{23} - C_{12}C_{33})}{D}\sigma_{11} + \frac{(C_{11}C_{33} - C_{13}^2)}{D}\sigma_{22} + \frac{(C_{12}C_{13} - C_{11}C_{23})}{D}\sigma_{33}$$

$$\varepsilon_{33} = \frac{\begin{pmatrix} C_{11} & C_{12} & \sigma_{11} \\ C_{12} & C_{22} & \sigma_{22} \\ C_{13} & C_{23} & \sigma_{33} \end{pmatrix}}{\begin{pmatrix} C_{11} & C_{12} & C_{13} \\ C_{12} & C_{22} & C_{23} \\ C_{13} & C_{23} & C_{33} \end{pmatrix}} = \frac{(C_{12}C_{23} - C_{13}C_{22})}{D}\sigma_{11} + \frac{(C_{12}C_{13} - C_{11}C_{23})}{D}\sigma_{22} + \frac{(C_{11}C_{22} - C_{12}^2)}{D}\sigma_{33}$$

$$\varepsilon_{12} = \frac{1}{2C_{66}}\sigma_{12} \ , \ \varepsilon_{13} = \frac{1}{2C_{55}}\sigma_{13} \ , \ \varepsilon_{23} = \frac{1}{2C_{44}}\sigma_{23}$$

(A-6)

Where D equals,

$$D = \begin{pmatrix} C_{11} & C_{12} & C_{13} \\ C_{12} & C_{22} & C_{23} \\ C_{13} & C_{23} & C_{33} \end{pmatrix} = C_{11}C_{22}C_{33} + 2C_{12}C_{13}C_{23} - C_{11}C_{23}^2 - C_{22}C_{13}^2 - C_{33}C_{12}^2$$

Compare with the equation of A-5, we can get that,

$$S_{11} = \frac{C_{22}C_{33} - C_{23}^2}{D}, \ S_{12} = \frac{C_{13}C_{23} - C_{12}C_{33}}{D} \ , \ S_{13} = \frac{C_{12}C_{23} - C_{13}C_{22}}{D}$$

$$S_{22} = \frac{C_{11}C_{33} - C_{13}^2}{D}, \ S_{23} = \frac{C_{12}C_{13} - C_{11}C_{23}}{D} \ , \ S_{33} = \frac{C_{11}C_{22} - C_{12}^2}{D}$$

$$S_{44} = \frac{1}{C_{44}} \ , \ S_{55} = \frac{1}{C_{55}} \ , \ S_{66} = \frac{1}{C_{66}}$$

(A-7)

Consider a VTI material with a hexagonal symmetry, we have five independent elastic constants,

$$C_{11} = C_{22} \ , \ C_{13} = C_{23} \ , \ C_{44} = C_{55} \ , \ C_{66} = \frac{1}{2}(C_{11} - C_{12}) \qquad \text{(A-8)}$$

The results A-7 can be written as,

$$S_{11} = S_{22} = \frac{C_{11}C_{33} - C_{13}^2}{D}, \ S_{12} = \frac{C_{13}^2 - C_{12}C_{33}}{D} \ ,$$

$$S_{13} = S_{23} = -\frac{2C_{66}C_{13}}{D}, \quad S_{33} = \frac{C_{11}^2 - C_{12}^2}{D}$$

$$S_{44} = S_{55} = \frac{1}{C_{44}} \ , \ S_{66} = 2(S_{11} - S_{12}) = \frac{1}{C_{66}}$$

$$D = C_{11}^2 C_{33} + 2C_{12}C_{13}^2 - 2C_{11}C_{13}^2 - C_{33}C_{12}^2 = 2C_{66}[C_{33}(C_{11} + C_{12}) - 2C_{13}^2]$$

(A-9)

The Young's modulus, E is defined as the ratio of extensional stress to extentional strain in a uniaxial stress state. While the Poisson's ratio, ν is defined as minus the ratio of lateral strain to axial strain in an uniaxial stress state. In a case of an orthorhombic type of symmetry, the elastic compliance has the form of A-3, where Sjj with j=4,5,6 relates shear strain to shear stress (Hearmon, 1961) and Sij with i, j =1,2,3 can be presented in terms of the Young's modulus and Poisson's ratio as (Christensen, 1982),

$$\nu_{mn} = \begin{cases} \nu_{12} = -S_{12}E_{11}, & \nu_{13} = -S_{13}E_{11}, \\ \nu_{21} = -S_{12}E_{22}, & \nu_{23} = -S_{23}E_{22}, \quad m, n = 1,2,3 \\ \nu_{31} = -S_{13}E_{33}, & \nu_{32} = -S_{23}E_{33} \qquad m \neq n \end{cases} \qquad \text{(A-10)}$$

$$E_{11} = \frac{1}{S_{11}}, \ E_{22} = \frac{1}{S_{22}}, \ E_{33} = \frac{1}{S_{33}} \qquad \text{(A-11)}$$

With the results in A-9, we can get the formulae for the Young's modulus and Poisson's ratio in terms of elastic constants as

$$\nu_{12} = \frac{C_{33}C_{12} - C_{13}C_{23}}{C_{33}C_{22} - C_{23}^2}, \quad \nu_{21} = \frac{C_{33}C_{12} - C_{13}C_{23}}{C_{33}C_{11} - C_{13}^2}$$

$$\nu_{13} = \frac{C_{22}C_{13} - C_{12}C_{23}}{C_{22}C_{33} - C_{23}^2}, \quad \nu_{23} = \frac{C_{11}C_{23} - C_{13}C_{12}}{C_{11}C_{33} - C_{13}^2}$$

$$\nu_{31} = \frac{C_{22}C_{13} - C_{12}C_{23}}{C_{22}C_{11} - C_{12}^2}, \quad \nu_{32} = \frac{C_{11}C_{23} - C_{13}C_{12}}{C_{11}C_{22} - C_{12}^2}$$

(A-12)

$$E_{11} = C_{11} - C_{13}\frac{C_{22}C_{13} - C_{12}C_{23}}{C_{22}C_{33} - C_{23}^2} - C_{12}\frac{C_{33}C_{12} - C_{13}C_{23}}{C_{22}C_{33} - C_{23}^2}$$

$$E_{22} = C_{22} - C_{23}\frac{C_{11}C_{23} - C_{12}C_{13}}{C_{11}C_{33} - C_{13}^2} - C_{12}\frac{C_{33}C_{12} - C_{13}C_{23}}{C_{11}C_{33} - C_{13}^2}$$

$$E_{33} = C_{33} - C_{23}\frac{C_{11}C_{23} - C_{12}C_{13}}{C_{11}C_{22} - C_{12}^2} - C_{13}\frac{C_{22}C_{13} - C_{12}C_{23}}{C_{11}C_{22} - C_{12}^2} \tag{A-13}$$

For VTI material with hexagonal symmetry, A-10, and A-11 can be simplified as,

$$\nu_{12} = -\frac{S_{12}}{S_{11}},\ \nu_{13} = -\frac{S_{13}}{S_{11}},\ \nu_{31} = -\frac{S_{13}}{S_{33}} \tag{A-14}$$

$$E_{11} = E_{22} = \frac{1}{S_{11}} = \frac{1}{S_{22}},\ E_{33} = \frac{1}{S_{33}} \tag{A-15}$$

With the results in A-9, we can get the formulae for the Young's modulus and Poisson's ratio in terms of elastic constants as (Banik, 2012),

$$\nu_{12} = -\frac{S_{12}}{S_{11}} = \frac{C_{33}C_{12} - C_{13}^2}{C_{33}C_{11} - C_{13}^2}$$

$$\nu_{13} = -\frac{S_{13}}{S_{11}} = \frac{C_{13}(C_{11} - C_{12})}{C_{11}C_{33} - C_{13}^2}$$

$$\nu_{31} = -\frac{S_{13}}{S_{33}} = \frac{C_{13}}{C_{11} + C_{12}} \tag{A-16}$$

$$E_{11} = E_{22} = \frac{1}{S_{11}} = \frac{1}{S_{22}} = 4C_{66}(1 - \frac{C_{33}C_{66}}{C_{11}C_{33} - C_{13}^2})$$

$$E_{33} = \frac{1}{S_{33}} = C_{33} - \frac{C_{13}^2}{C_{11} - C_{66}} \tag{A-17}$$

For cubic case, as $C_{11}=C_{22}=C_{33}$, $C_{12}=C_{13}=C_{23}$, and $C_{44}=C_{55}=C_{66}$, so the formulae can be simplified as,

$$\nu = \frac{C_{12}}{C_{11} + C_{12}} \tag{A-18}$$

$$E = C_{11} - \frac{2C_{12}^2}{C_{11} + C_{12}} \tag{A-19}$$

Please note that cubic symmetry attains the same values along principal axes. The anisotropy exists in other directions to the principal axes.

While for isotropic case, as $C_{11}=C_{22}=C_{33}$, $C_{12}=C_{13}=C_{23}$, and $C_{44}=C_{55}=C_{66}=(C_{11}-C_{12})/2$, so the formulae are the same as cubic symmetry for both Young's modulus and Poisson's ratio,

$$\nu = \frac{C_{12}}{C_{11} + C_{12}} \tag{A-20}$$

$$E = C_{11} - \frac{2C_{12}^2}{C_{11} + C_{12}} \tag{A-21}$$

We summarize the results for the three types of symmetry in below table (Table A-1),

Table A-1 Anisotropic forms of Young's modulus and Poisson's ratio.

	Orthorhombic	VTI	Isotropic / Cubic
E_{11}	$C_{11}-C_{13}\dfrac{C_{22}C_{13}-C_{12}C_{23}}{C_{22}C_{33}-C_{23}^2}-C_{12}\dfrac{C_{33}C_{12}-C_{13}C_{23}}{C_{22}C_{33}-C_{23}^2}$	$4C_{66}\left(1-\dfrac{C_{33}C_{66}}{C_{11}C_{33}-C_{13}^2}\right)$	$C_{11}-\dfrac{2C_{12}^2}{C_{11}+C_{12}}$
E_{22}	$C_{22}-C_{23}\dfrac{C_{11}C_{23}-C_{12}C_{13}}{C_{11}C_{33}-C_{13}^2}-C_{12}\dfrac{C_{33}C_{12}-C_{13}C_{23}}{C_{11}C_{33}-C_{13}^2}$		
E_{33}	$C_{33}-C_{23}\dfrac{C_{11}C_{23}-C_{12}C_{13}}{C_{11}C_{22}-C_{12}^2}-C_{13}\dfrac{C_{22}C_{13}-C_{12}C_{23}}{C_{11}C_{22}-C_{12}^2}$	$C_{33}-\dfrac{C_{13}^2}{C_{11}-C_{66}}$	
ν_{12}	$\dfrac{C_{33}C_{12}-C_{13}C_{23}}{C_{33}C_{22}-C_{23}^2}$	$\dfrac{C_{33}C_{12}-C_{13}^2}{C_{33}C_{11}-C_{13}^2}$	$\dfrac{C_{12}}{C_{11}+C_{12}}$
ν_{21}	$\dfrac{C_{33}C_{12}-C_{13}C_{23}}{C_{33}C_{11}-C_{13}^2}$		
ν_{13}	$\dfrac{C_{22}C_{13}-C_{12}C_{23}}{C_{22}C_{33}-C_{23}^2}$	$\dfrac{C_{13}(C_{11}-C_{12})}{C_{11}C_{33}-C_{13}^2}$	
ν_{23}	$\dfrac{C_{11}C_{23}-C_{13}C_{12}}{C_{11}C_{33}-C_{13}^2}$		
ν_{31}	$\dfrac{C_{22}C_{13}-C_{12}C_{23}}{C_{22}C_{11}-C_{12}^2}$	$\dfrac{C_{13}}{C_{11}+C_{12}}$	
ν_{32}	$\dfrac{C_{11}C_{23}-C_{13}C_{12}}{C_{11}C_{22}-C_{12}^2}$		

Appendix B: The Green's function in GSA method

The equation (5-29) of effective elastic constants in heterogeneous anisotropic media can be expressed using the GSA method as (Bayuk and Chesnokov, 1998),

$$C^{*} = \left\{\sum_{i=1}^{n} v_i C_i \int P_i(\chi_i;\theta,\phi,\psi)\left[I - g_i(C_i - C^c)\right]^{-1} \sin\theta d\chi_i d\theta d\phi d\psi\right\} \times$$
$$\left\{\sum_{i=1}^{n} v_i \int P_i(\chi_i;\theta,\phi,\psi)\left[I - g_i(C_i - C^c)\right]^{-1} \sin\theta d\chi_i d\theta d\phi d\psi\right\}^{-1} \quad \text{(B-1)}$$

Where C_i and V_i are the stiffness tensor and volume concentration of the i^{th} component. I is the 4^{th} rank tensor. C^c is the tensor of comparison body. g is Green's tensor, which is determined by the properties of the comparison body and shape of the inclusions. θ, Φ, and ψ are the Euler angles.

In the elasticity case, the expression of Green's tensor g has a definite form for certain inclusions (Bayuk et al., 2007). For ellipsoidal inclusions in a spherical coordinate system, it can be expressed as:

$$\begin{aligned} g_{ijkl}(x) &= \frac{(a_{kj,il} + a_{ki,jl} + a_{lj,ik} + a_{li,jk})}{4} \\ a_{kj,il} &= -\frac{1}{4\pi}\int_{-\infty}^{\infty} n_{kj}\Lambda_{il}^{-1} d\Omega \end{aligned} \quad \text{(B-2)}$$

Where

$$\begin{aligned} \Lambda_{il} &= C_{ijkl}^{c} n_{jk} \\ d\Omega &= \sin\theta d\theta d\varphi \end{aligned} \quad \text{(B-3)}$$

C^c is the stiffness tensor of comparison body. At the range of the polar angle $\theta \in [0,\pi]$

and the azimuthal angle $\varphi \in [0,2\pi]$, The equation will be,

$$g_{ijkl} = -\frac{1}{16\pi}\int_0^{2\pi}\int_0^{\pi}(n_{kj}\Lambda_{il}^{-1} + n_{ki}\Lambda_{jl}^{-1} + n_{lj}\Lambda_{ik}^{-1} + n_{li}\Lambda_{jk}^{-1})\sin\theta d\theta d\varphi \quad \text{(B-4)}$$

Where

$$\begin{aligned} n_{kj} &= n_k n_j \\ n_1 &= \sin\theta\cos\varphi / a_1 \\ n_2 &= \sin\theta\sin\varphi / a_2 \\ n_3 &= \cos\theta / a_3 \end{aligned} \quad \text{(B-5)}$$

a1, a2, and a3 are the semi-axes of the abitrary ellipsoidal inclusion. In the general case, a1 $\neq$ a2 $\neq$ a3, which can be used to approximate the shape of pores, such as spherical, penny-shaped, needle-shaped and so on.

For transport case, the expression of Green's tensor g can be expressed as:

$$g_{ij} = -\frac{1}{4\pi}\int_0^{2\pi}\int_0^{\pi} n_{ij}\Lambda^{-1}\sin\theta d\theta d\varphi \quad \text{(B-6)}$$

where $\Lambda = T_{ij}^{c} n_{ij}$, and n1, n2, and n3 have the same form as equation (B-5). T_{ij}^{c} is the effective permeability or conductivity of the comparison body.

REFERENCES

Alderson, A., and Evans, K. E., 2002, Molecular origin of auxetic behavior in tetrahedral framework silicates. Physical Review Letters, 89, 5301-5304.

Alexandrov,K. S., and T.V. Ryzhova, 1961, Elastic properties of rock-forming minerals II. Layered silicates. Bulletin of the Academy of Sciences of the U.S.S.R., Geophysics Series, 9, 1165–1168.

Banik, N., and M. Egan, 2012, Effects of VTI anisotropy on shale reservoir characterization. SPE Middle East Unconventional Gas Conference and Exhibition, 150269.

Bass, J., 1995, Minerals Physics and Crystallography: A Handbook of Physical Constants. AGU, 46-59.

Baughman, R. H., Socrates, S. O., Stafstrom, S., Zakhidov, A. A., Mitchell, T. B., and Dubin, D. H. E., 2000, Negative Poisson's ratios for extreme states of matter. Science, 288, 2018-2022.

Bayuk, I. O., and Chesnokov, E. M., 1997, Experimental and theoretical study of sedimetary rock properties. SEG Expanded Abstract, 984–986.

Bayuk, I., and Chesnokov, E., 1998, Correlation between elastic and transport properties of porous cracked anisotropic media. Journal of Physics and Chemistry of the Earth, 23, 361–366.

Bayuk, I., M. Ammerman, E. M. Chesnokov, 2007, Elastic moduli of anisotropic clay. Geophysics, 72, D107–117.

Belikov, B.P., Alexandrov, K., and Ryzhova, T.V., 1970. Elastic Properties of Rock-Forming Minerals and Rocks. Nauka, Russia, 276.

Biot, M. A., 1941, General theory of three-dimensional consolidation. Journal of Applied Physics, 12, 155-164.

Bustin, R.M., Bustin A.M.M., Cui X, Ross D.J.K, and Murthy Pathi V.S., 2008, Impact of shale properties on pore structure and storage characteristics. SPE Shale Gas Production Conference, 119892.

Castagna, J.P., Batzle, M.L. and Eastwood, R.L., 1985, Relationships between compressional wave and shear-wave velocities in clastic silicate rocks. Geophysics, 50, 571-581.

Castagna, J. P., Batzle, M. L., and Kan, T. K., 1993, Rock physics – The link between rock properties and AVO response, in Offset-Dependent Reflectivity – Theory and Practice of AVO Analysis. Society of Exploration Geophysicists, 135-171.

Christensen, R.M., 1982, Theory of viscoelasticity: an introduction. Academic Press, New York.

Christensen, N., and Johnston, J., 1995, Seismic anisotropy of shales. Journal of Geophysical Research, 100, 5991–6003.

Chesnokov, E., I. Bayuk, and M. Ammerman, 2010, Determination of shale stiffness tensor from standard logs. Geophysical Prospecting, 58, 1063–1082.

Civan, F., 2010a, Effective correlation of apparent gas permeability in tight porous media, Transport in Porous Media, 82, 375-384.

Civan, F., 2010b, A review of approaches for describing gas transfer through extremely tight porous media. The Third ECI International Conference on Porous Media and its Applications in Science, 1254, 53-58.

Dellinger, J., and L. Vernik, 1994, Do travel times in pulse transmission experiments yield anisotropic group or phase velocities?. Geophysics, 59, 1774–1779.

Di Chen, 2012, Modeling Elastic Properties of Gas Shale and Microstructure Study on Barnett Shale. unpublished thesis, University of Houston, 39.

Dyaur, N., Bayuk I., Mohamed Y., and Chesnokov, E., 2008, Anisotropy and elastic constants of the shale samples under unloaded conditions. 13th International workshop on Seismic Anisotropy.

Eshelby, J. D., 1957, The determination of the elastic field of an ellipsoidal inclusion and related problems. Proceedings of the Royal Society of London, 241, 376–396.

Goloshubin, G., D. Silin, V. Vingalov, G. Takkand, and M. Latfullin, 2008, Reservoir permeability from seismic attribute analysis. The Leading Edge, 27, 376–381.

Hearmon, R.F.S., 1961, Introduction to applied anisotropic elasticity. Oxford University Press, London.

Hornby, B. E., Schwartz, L. M., and Hudson, J. A., 1994, Anisotropic effective-medium modeling of the elastic properties of shales. Geophysics, 59, 1570–1583.

Hudson, J. A., 1981, Wave speed and attenuation of elastic waves in material containing cracks. Geophysical Journal of the Royal Astronomical Society, 64, 133–150.

Li, Y., 2006, An empirical method for estimation of anisotropic parameters in clastic rocks. The Leading Edge, 25, 706-711.

Love, A. E. H., 1927, A Treatise on the Mathematical Theory of Elasticity, 4th edition. Cambridge University Press, 643.

Lu, K., Dyaur, N., Mohamed Y., and Chesnokov, E., 2015, Barnett Shale Velocity and Permeability Anisotropy Measurement. Quarterly Physics Review, 2, 201-235.

Mavko, G., T. Mukerji, and J. Dvorkin, 1998, The rock physics handbook. Cambridge University Press.

Metwally, Y.M., and Chesnokov, E., 2010, Measuring gas shale permeability tensor in the lab scale. SEG Expanded Abstract, 2628-2633.

Metwally YM, Sondergeld CH., 2011, Measuring low permeabilities of gas-sands and shales using a pressure transmission technique. International Journal of Rock Mechanics and Mining Sciences, 48, 1135-1144.

Müller, T. M., B. Gurevich, and M. Lebedev, 2010, Seismic wave attenuation and dispersion resulting from wave-induced flow in porous rocks — A review. Geophysics, 75, 147–164.

Montgomery, S. L., D. M. Jarvie, K. A. Bowker, and R. M. Pollastro, 2005, Mississippian Barnett Shale, Fort Worth Basin, northcentral Texas: Gas-shale play with multi-trillion cubic foot potential. AAPG Bulletin, 89, 155–175.

Peselnick, L., and Robie, R., 1963, Elastic constants of calcite. Journal of Applied Physics, 34, 2494–2495.

Sone H., Zoback, M.D., 2013, Mechanical properties of shale-gas reservoir rocks - Part 1: Static and dynamic elastic properties and anisotropy. Geophysics, 78, 381–392.

Sondergeld C. H., Rai C., Margesson R., and Whitten, K., 2000, Ultrasonic measurement of anisotropy on the Kimmeridge Shale. SEG Expanded Abstract, 1858-1861.

Shermergor, T. D., 1977, Theory of elasticity of inhomogeneous media. Nanka, Moscow (in Russian).

Tao Jiang, 2013, Connection of Elastic and Transport Properties: Effective Medium Study in Anisotropic Porous Media. unpublished dissertation, University of Houston, 8.

Timoshenko, S.P. and Goodier, J.N., 1934. Theory of Elasticity. New York: McGraw-Hill, 6.

Thomsen L, 1986, Weak elastic anisotropy. Geophysics, 51, 1954–66.

Thomsen, L., 1990, Poisson was not a geophysicist. The Leading Edge, 9, 27–29.

Tsuneyama, F., and Mavko, G., 2005, Velocity anisotropy estimation for brine-saturated sandstone and shale. The Leading Edge, 24, 882-888.

Vernik, L., and Nur, A., 1992, Ultrasonic velocity and anisotropy of hydrocarbon source rocks. Geophysics, 57, 727–735.

Vernik, L., and Liu, X., 1997, Velocity anisotropy in shales: A petrophyscial study. Geophysics, 62, 521-532.

Vernik, L., Fisher, D., and Bahret, S., 2002, Estimation of net-to-gross from P and S impedance in deepwater turbidites. The Leading Edge, 21, 380-387.

Vernik, L., and Milovac, J., 2011, Rock physics of organic shales. The Leading Edge, 30, 318-323.

Wang, Z., 2002, Seismic anisotropy in sedimentary rocks, part 1: A single-plug laboratory method. Geophysics, 67, 1415–1422.

Willis, J. R., 1977, Bounds and self-consistent estimates for the overall properties of anisotropic composites. Journal of the Mechanics and Physics of Solids, 25, 185–202.

Yan, F., D.-H. Han, and Q. Yao, 2012, Oil shale anisotropy measurement and sensitivity analysis. SEG Expanded Abstracts, 1-5.